0090-9556/05/3312-1785–1790$20.00
DRUG METABOLISM AND DISPOSITION
Copyright © 2005 by The American Society for Pharmacology and Experimental Therapeutics
DMD 33:1785–1790, 2005

Vol. 33, No. 12
6205/3062222
Printed in U.S.A.

GEFITINIB (IRESSA) INHIBITS THE CYP3A4-MEDIATED FORMATION OF 7-ETHYL-10-(4-AMINO-1-PIPERIDINO)CARBONYLOXYCAMPTOTHECIN BUT ACTIVATES THAT OF 7-ETHYL-10-[4-*N*-(5-AMINOPENTANOIC ACID)-1-PIPERIDINO]CARBONYLOXYCAMPTOTHECIN FROM IRINOTECAN

Ken-ichi Fujita, Yuichi Ando, Masaru Narabayashi, Toshimichi Miya, Fumio Nagashima, Wataru Yamamoto, Keiji Kodama, Kazuhiro Araki, Hisashi Endo, and Yasutsuna Sasaki

Department of Clinical Oncology, Saitama Medical School, Saitama, Japan

Received June 22, 2005; accepted August 25, 2005

ABSTRACT:

Gefitinib (Iressa) is an anticancer drug that selectively inhibits tyrosine kinases of epidermal growth factor receptor. Gefitinib might affect CYP3A4-mediated metabolism, since the drug is a substrate of human CYP3A. In this study, we evaluated the effects of gefitinib on drug metabolism catalyzed by human CYP3A4. The effects of gefitinib on the CYP3A4-mediated formation of NPC (7-ethyl-10-(4-amino-1-piperidino)carbonyloxycamptothecin) and that of APC (7-ethyl-10-[4-*N*-(5-aminopentanoic acid)-1-piperidino]carbonyloxycamptothecin) from irinotecan were examined with the use of human liver and small intestinal microsomes. Gefitinib inhibited the formation of NPC in liver and small intestinal microsomes. The apparent intrinsic metabolic clearance (CL_{int}) in the presence of 40 μM gefitinib was equivalent to about 26% of control in liver microsomes and 45% of control in small intestinal microsomes. Gefitinib stimulated the formation of APC by CYP3A4. CL_{int} in the presence of 20 μM gefitinib with human liver microsomes was about 1.9 times higher than control. In human small intestinal microsomes, APC formation was enhanced by the addition of gefitinib at concentrations 20 μM or higher. CL_{int} in the presence of 40 μM gefitinib was 2.8 times higher than control. Thus, we discovered that gefitinib inhibited the formation of NPC but stimulated the formation of APC from irinotecan.

Gefitinib (Iressa) is a member of a new class of oral drugs used to treat locally advanced or metastatic non-small cell lung cancer (NSCLC) (Cohen et al., 2004). This drug is a synthetic anilinoquinazoline derivative that selectively inhibits tyrosine kinases of epidermal growth factor receptor. Gefitinib reversibly competes with ATP at a critical ATP-binding site within epidermal growth factor receptor protein (Ward et al., 1994; Barker et al., 2001).

Previous studies have shown that gefitinib is metabolized by CYP3A4 (Cully and Faulds, 2002; Cohen et al., 2004; McKillop et al., 2005). Cytochrome P450 is a heme-containing enzyme that catalyzes the oxidation of a wide variety of endogenous and exogenous compounds, including drugs, carcinogens, and other xenobiotic chemicals (Nelson et al., 1996). CYP3A4 is the most abundant cytochrome P450 expressed in the human liver as well as in the small intestine. This cytochrome participates in the metabolism of 25% of all therapeutic drugs or 50% of therapeutic drugs undergoing biotransformation. In general, modulation of a drug-metabolizing enzyme by a given drug alters the pharmacokinetics of other drug(s) metabolized by the enzyme, leading to drug interaction(s). Various interactions resulting from drug metabolism by CYP3A4 have been reported (Honig et al., 1993a,b,c). Gefitinib may also affect the CYP3A4-mediated metabolism of other substrates such as steroids (Gentile et al., 1996) and antiemetic agents (Villikka et al., 1999), which are simultaneously used with gefitinib to improve treatment- and disease-related symptoms in patients with cancer. Besides affecting the CYP3A4-mediated metabolism of concurrently administered supportive medication, gefitinib may influence the CYP3A4-mediated metabolism of irinotecan (7-ethyl-10[4-(1-piperidino)-1-piperidino]carbonyloxycamptothecin) as described below. Irinotecan is a camptothecin analog with potent antitumor activity resulting from inhibition of topoisomerase I. It is widely used for the treatment of colorectal and lung cancers (Negoro et al., 1991; Kudoh et al., 1998; Rougier et al., 1998). Irinotecan is metabolized by carboxylesterases to form SN-38 (7-ethyl-10-hydroxycamptothecin), an active metabolite (Mathijssen et al., 2003), as well as by CYP3A4 to produce the nonactive metabolites NPC (7-ethyl-10-(4-amino-1-piperidino)carbonyloxycamptothecin) and APC (7-ethyl-10-[4-N-(5-aminopentanoic acid)-1-piperidino]carbonyloxycamptothecin) (Haaz et al., 1998a,b; Santos et al., 2000) (Fig. 1). Mathijssen et al. (2004) have shown that CYP3A4 phenotype as determined by midazolam clearance significantly correlates with irinotecan clearance, indicating that CYP3A4 has an essential role in the metabolism of irinotecan in humans. Since gefitinib and irinotecan are used for the treatment of NSCLC and have different mechanisms of action, these drugs may act synergistically. Gefitinib and irinotecan

This study was supported in part by a Grant-in-Aid from the Ministry of Health and Welfare of Japan (13-10).

Article, publication date, and citation information can be found at http://dmd.aspetjournals.org.

doi:10.1124/dmd.105.006205.

ABBREVIATIONS: NSCLC, non-small cell lung cancer; SN-38, 7-ethyl-10-hydroxycamptothecin; NPC, 7-ethyl-10-(4-amino-1-piperidino)carbonyloxycamptothecin; APC, 7-ethyl-10-[4-*N*-(5-aminopentanoic acid)-1-piperidino]carbonyloxycamptothecin; HPLC, high-performance liquid chromatography; DMSO, dimethyl sulfoxide; CL_{int}, metabolic intrinsic clearance.

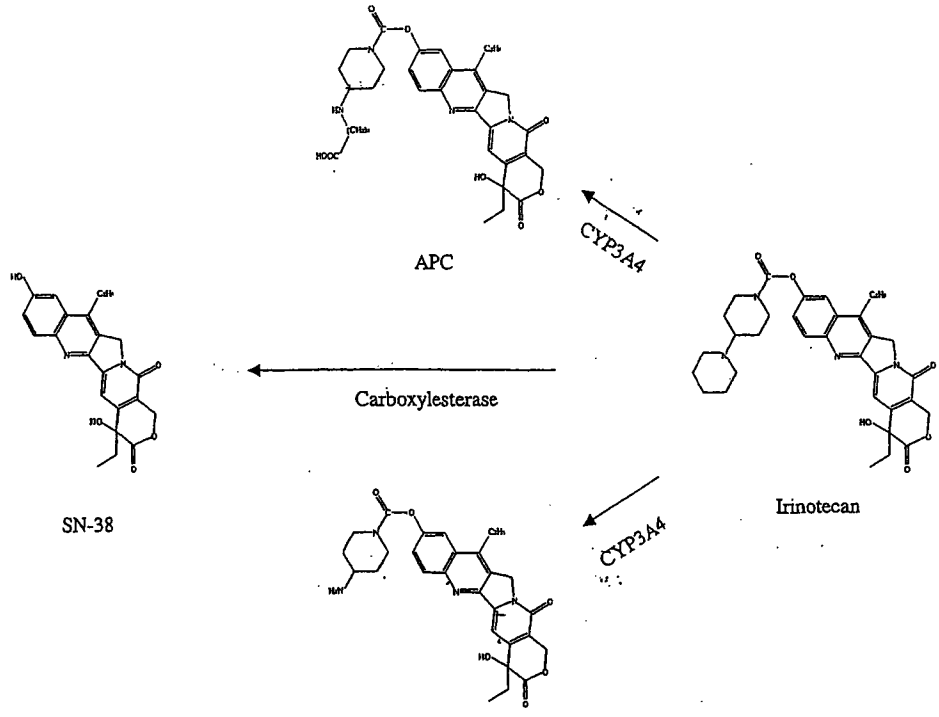

FIG. 1. Major metabolic pathways for irinotecan.

may thus be used concurrently for the treatment of NSCLC in the future. Stewart et al. (2004) have suggested that gefitinib may affect the CYP3A-mediated metabolism of irinotecan. They investigated the effects of gefitinib on the pharmacokinetics of orally administered irinotecan in mice. When administered concurrently with irinotecan, gefitinib was found to increase the oral bioavailability of irinotecan and to subsequently increase the plasma concentration of SN-38. They concluded that gefitinib might inhibit ABCG2 transporter, prominently expressed on the apical side of enterocytes. ABCG2 transporter is considered to play a crucial role in the efflux of irinotecan, thereby increasing its oral bioavailability. However, an alternative hypothesis proposes that gefitinib, a substrate of CYP3A (Culy and Faulds, 2002; Cohen et al., 2004; McKillop et al., 2005), inhibits irinotecan metabolism catalyzed by mouse CYP3A present in the liver and small intestine (Sakuma et al., 2000; Zhang et al., 2003), thus increasing the bioavailability of irinotecan and consequently elevating the plasma concentration of SN-38. In humans, low bioavailability of orally administered irinotecan (8–24%) was observed in some phase I trials, suggesting the high first-pass effects probably in the small intestine and the liver (Kuppens et al., 2004).

This study focused on the effects of gefitinib on the CYP3A4-mediated formation of NPC and APC from irinotecan. Human liver and small intestinal microsomes were used in vitro to investigate the effects of gefitinib on the CYP3A4-catalyzed metabolism of irinotecan.

Materials and Methods

Chemicals. 1′-Hydroxymidazolam, midazolam hydrochloride, and pooled human liver microsomes [catalog number 452161(H161)] were purchased from Daiichi Pure Chemicals (Tokyo, Japan). The pool comprised 22 specimens (21 white and 1 Hispanic). Microsomes were diluted in 250 mM sucrose. Testosterone 6β-hydroxylase activity of the liver microsomes, measured by BD Gentest (Woburn, MA), was 6800 pmol/min/mg protein. There was no information on CYP3A5. Human small intestinal microsomes (catalog number H0610.I) were obtained from Xenotech (Lenexa, KA). The pool was comprised of 11 specimens (9 white and 2 African American). Microsomes were diluted in 250 mM sucrose. Aprotinin, leupeptin, and phenylmethylsulfonyl fluoride were used in the preparation of the microsomes. No information was described on CYP3A5. Irinotecan, NPC, and APC were gifts from Yakult (Tokyo, Japan). Gefitinib was obtained from AstraZeneca (London, UK). All chemicals and solvents were of the highest grade commercially available.

Assay of NPC and APC Formation Catalyzed by Human CYP3A4. The amounts of NPC and APC formed by reactions catalyzed by human CYP3A4 were assayed as described by Haaz et al. (1998a,b), with minor modifications. Briefly, the incubation mixture consisted of 100 mM sodium potassium phosphate buffer (pH 7.4), 50 μM EDTA disodium salt, an NADPH-generating system (0.5 mM $NADP^+$, 5 mM $MgCl_2$, 5 mM glucose 6-phosphate, and 1 unit/ml glucose-6-phosphate dehydrogenase), and microsomal fractions of human liver or human small intestine in a final volume of 0.25 ml. When human liver microsomes were used, the protein content and reaction time were predetermined with 80 μM irinotecan based on the linearity between t' microsomal protein concentration (up to 0.133 mg/ml) and the reaction ti. (up to 10 min) versus the rate of metabolite formation. On the basis of the results, the protein content and the reaction time were determined to be 0.133 mg/ml and 10 min, respectively. When human small intestinal microsomes were used, linearity was obtained up to a microsomal protein concentration of 0.375 mg/ml and an incubation time of 20 min with 80 μM irinotecan. On the basis of these results, the protein content and reaction time were set at 0.375 mg/ml and 20 min, respectively. The NPC and APC metabolites were analyzed by HPLC using a computerized HPLC system (Hitachi model 7000 series; Hitachi, Tokyo, Japan) equipped with a TSK-gel ODS-120T analytical column (4.6 × 250 mm, 4 μm; Tosoh, Tokyo, Japan). The mobile phase consisted of 75 mM ammonium acetate (pH 4.0) for solvent A and acetonitrile for solvent B. The metabolites were separated using a linear gradient of 85% to 65% solvent A, a time of 0 to 20 min, and a flow rate of 1.0 ml/min. The metabolites were quantified by comparing the HPLC peak area to that of the internal standard. Lower limits of quantification were 0.56 nM for NPC and 0.48 nM for APC, respectively. The intra- and interassay coefficient variations at 4.5 nM for NPC and 3.8 nM for APC were under 12% and 7.9%, respectively.

Effects of Gefitinib on NPC and APC Formation by CYP3A4. The effects of gefitinib on the CYP3A4-mediated metabolism of irinotecan to form the respective metabolites NPC and APC were investigated as follows. After

preincubation of the incubation mixture with gefitinib at 37°C for 5 min, the substrate irinotecan was added (final concentration of 20 μM). Irinotecan was used as lactone (stock diluted in 0.01 M citric acid, pH 3.0). Gefitinib was dissolved in DMSO. The final concentration of the solvent in the reaction mixture was 1%. The reaction was performed as described above. The effects of gefitinib on the CYP3A4-catalyzed metabolism of irinotecan were expressed as a percentage of activity as compared with control in the absence of an effector. Control experiments were performed with the representative CYP3A4 inhibitors ketoconazole and erythromycin and a typical stimulator, α-naphthoflavone. Each chemical was dissolved in DMSO. The final concentration of the solvent in the incubation mixture was 1%. Each assay was performed three times in duplicate.

Enzyme Kinetics. The concentrations of irinotecan and gefitinib ranged from 5 to 80 μM and 5 to 40 μM, respectively. Data points were fitted to the Michaelis-Menten equation by nonlinear least-squares regression analysis with the use of Origin 7.5 software (OriginLab Corp., Northampton, MA). The V_{max}/K_m value represented the metabolic intrinsic clearance (CL_{int}).

Assay of Midazolam 1′-Hydroxylase Activity of Human CYP3A. Midazolam 1′-hydroxylase activity of human CYP3A was assayed by our method (Fujita et al., 2003), with minor modifications. Briefly, a typical incubation mixture consisted of 100 mM sodium potassium phosphate buffer (pH 7.4), 50 μM EDTA disodium salt, an NADPH-generating system (0.5 mM $NADP^+$, 5 mM MgCl2, 5 mM glucose 6-phosphate, and 1 unit/ml glucose-6-phosphate dehydrogenase), and microsomal fraction of human liver in a final volume of 0.25 ml. The protein content and reaction time were predetermined with 10 μM midazolam based on linearity between the microsomal protein concentration (up to 0.16 mg/ml) and the reaction time (up to 4 min) versus the metabolite formation rate. On the basis of the results, the protein content and the reaction time were determined to be 0.16 mg/ml and 4 min, respectively. Reactions were initiated by the addition of midazolam and terminated by the addition of 2.5 ml of ethyl acetate. The 1′-hydroxymidazolam metabolite was analyzed by HPLC as described by us (Fujita et al., 2003).

Effects of Gefitinib on Midazolam 1′-Hydroxylase Activity of CYP3A. The effects of gefitinib on the midazolam 1′-hydroxylase activity of CYP3A were investigated as follows. After preincubation of the mixture with gefitinib at 37°C for 5 min, the substrate midazolam was added (final concentration of 10 μM). DMSO was used as a solvent to dissolve gefitinib. The final concentration of the solvent in the reaction mixture was 1%. The reaction was performed as described above. The effects of α-naphthoflavone on the midazolam 1′-hydroxylase activity of CYP3A were also examined as control. α-Naphthoflavone was also dissolved in DMSO. The final concentration of the solvent in the incubation mixture was 1%. The effect of gefitinib on midazolam 1′-hydroxylation was expressed as the percentage of activity as compared with control in the absence of an effector. Each assay was performed three times in duplicate.

Statistical Considerations. Statistical significance in the differences of NPC- and APC-producing activity or midazolam 1′-hydroxylase activity of CYP3A4 determined in the absence or the presence of an inhibitor or an activator was analyzed with a two-sample *t* test. All test results with $p < 0.05$ were regarded as statistically significant.

Results

Effects of Gefitinib on Irinotecan Metabolism by Human CYP3A4. The effects of gefitinib on the metabolism of irinotecan by CYP3A4 were evaluated. Table 1 shows the results obtained with human liver microsomes. Gefitinib had opposing effects on the formation of NPC and that of APC. The addition of gefitinib inhibited the formation of NPC but stimulated the formation of APC. The production of NPC and of APC in the presence of 40 μM gefitinib was 30.8% and 173% of the control value, respectively. No metabolite of gefitinib had a retention time similar to that of APC on the HPLC chromatogram after incubating the chemical alone with human liver microsomes (data not shown). The typical CYP3A4 inhibitors ketoconazole and erythromycin inhibited the formation of both NPC and APC from irinotecan. The representative CYP3A4 activator α-naphthoflavone (Shou et al., 1994; Harlow and Halpert, 1997; Koley et al., 1997) enhanced the production of both NPC and APC.

TABLE 1

Effects of gefitinib on NPC and APC formations by CYP3A4 in human liver or small intestinal microsomes

The concentration of irinotecan was 20 μM. The control activities of NPC and APC formation from irinotecan by CYP3A4 in the liver microsomes or in the small intestinal microsomes determined in the absence of an inhibitor or an activator were 34.2 and 8.63 pmol/min/mg protein or 3.14 and 1.32 pmol/min/mg protein.

Chemical	Concentration	NPC Formation[a]	APC Formation[a]
	μM	% of control	
Liver			
Gefitinib	40.0	30.8 ± 1.4[b]	173 ± 12[b]
Ketoconazole	1.0	4.31 ± 0.35[b]	5.31 ± 1.2[b]
Erythromycin	100.0	9.90 ± 1.2[b]	17.6 ± 2.8[b]
α-Naphthoflavone	5.0	151 ± 12[b]	313 ± 12[b]
Small Intestine			
Gefitinib	40.0	70.4 ± 3.6[b]	252 ± 24[b]
Ketoconazole	1.0	7.49 ± 0.92[b]	8.57 ± 0.23[b]
Erythromycin	100.0	19.4 ± 1.9[b]	23.2 ± 4.5[b]
α-Naphthoflavone	20.0	143 ± 4.0[b]	379 ± 16[b]

[a] Values are presented as mean ± S.D. ($n = 3$).
[b] Significant difference between values obtained in the presence or absence of an inhibitor or an activator ($P < 0.05$).

We also evaluated the effects of gefitinib on irinotecan metabolism in the presence of human small intestinal microsomes (Table 1). The formation of NPC and of APC in the presence of 40 μM gefitinib was 70.4% and 252% as compared with control, respectively. As expected, ketoconazole and erythromycin inhibited the formation of both NPC and APC. In contrast, α-naphthoflavone activated the production of both NPC and APC.

Kinetic Analysis. To investigate the effects of gefitinib on kinetic parameters of the CYP3A4-catalyzed formation of NPC and APC from irinotecan, reaction velocity versus substrate concentration was plotted in the presence or absence of gefitinib. The results obtained with human liver microsomes are shown in Fig. 2. Kinetic parameters were determined on the basis of the best fits of the velocity versus substrate concentration plots of Fig. 2 (Table 2).

The apparent K_m and V_{max} values for the formation of NPC were 44 μM and 128 pmol/min/mg protein, respectively. As shown in Table 2, CL_{int} for NPC formation decreased as the gefitinib concentration increased. The CL_{int} in the presence of 40 μM gefitinib was about 26% of that in the absence of gefitinib. A decrement in V_{max} contributed to a decrease in CL_{int} at gefitinib concentrations ranging from 0 to 20 μM. In contrast, an increment in the K_m value lowered the CL_{int} at a gefitinib concentration of 40 μM.

The K_m and V_{max} for the formation of APC were 68 μM and 46 pmol/min/mg protein, respectively. The CL_{int} was increased by the addition of gefitinib. The increment in CL_{int} seen at gefitinib concentration of 5 μM was caused by a decrease in the K_m value, whereas the increase at gefitinib concentrations ranging from 10 to 20 μM was by an increase of V_{max}. The maximum CL_{int} was observed in the presence of 20 μM gefitinib. The CL_{int} was about 1.9 times higher than the control value. The potential of gefitinib to increase CL_{int} decreased at gefitinib concentrations higher than 20 μM, since the K_m value simultaneously increased with the V_{max} value. K_i value of the inhibition of NPC formation by gefitinib was calculated to be 16 μM.

The effects of gefitinib on kinetic parameters for the formation of NPC and APC by CYP3A4 were also examined with human small intestinal microsomes. The reaction velocity versus the substrate concentration was plotted in the presence or absence of gefitinib. The results are shown in Fig. 3. The best fits of the velocity versus substrate concentration plots of Fig. 3 were used to determine the kinetic parameters (Table 3).

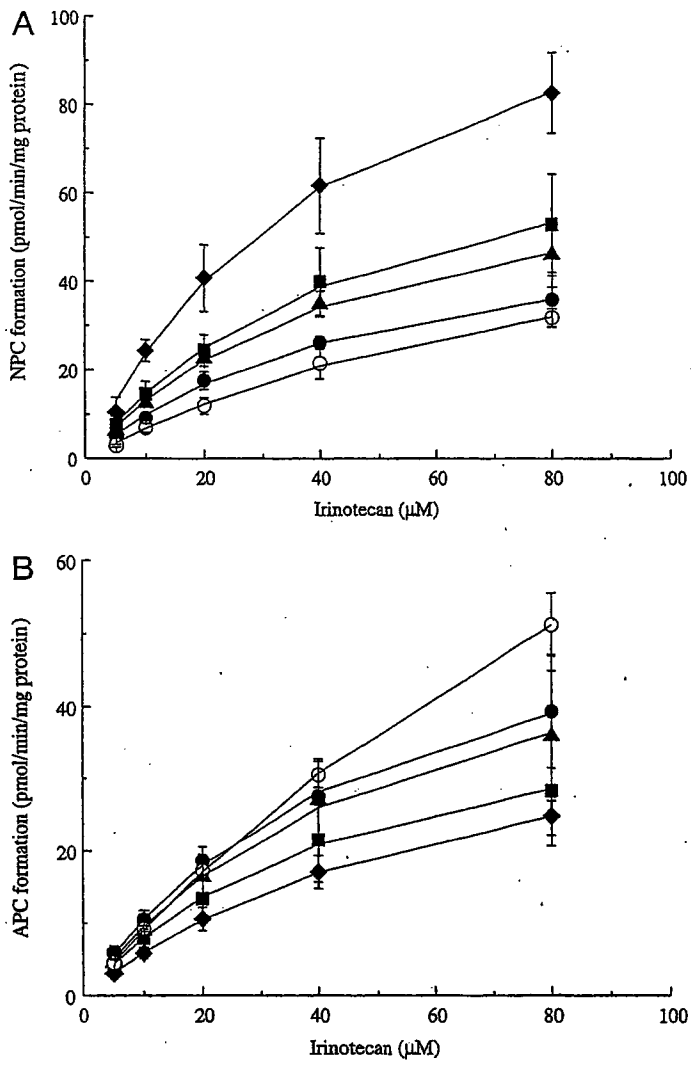

FIG. 2. Velocity versus substrate concentration plots for irinotecan metabolism by CYP3A4 in human liver microsomes. A, NPC formation; B, APC formation. Each data point represents the mean of triplicate determinations and is shown with standard deviation bars. ◇, 0 μM gefitinib; ■, 5 μM gefitinib; ▲, 10 μM gefitinib; ●, 20 μM gefitinib; ○, 40 μM gefitinib.

The apparent K_m and V_{max} values for the formation of NPC were 49 μM and 15 pmol/min/mg protein, respectively. Similar to the results with human liver microsomes, CL_{int} for NPC formation decreased as the gefitinib concentration increased (Table 3). The CL_{int} in the presence of 40 μM gefitinib was about 45% of that in the absence of gefitinib. An increment in the K_m value was associated with a decrease in the CL_{int}. The K_i value of the inhibition of NPC formation by gefitinib was 48 μM.

The K_m and V_{max} values for the formation of APC were 59 μM and 6.7 pmol/min/mg protein, respectively. There was no increase in CL_{int} when 5 or 10 μM gefitinib was added to the reaction mixture, since the K_m value increased despite a rise in the V_{max} value. The CL_{int} value for APC formation was increased by the addition of gefitinib at concentrations of 20 μM or higher. As the gefitinib concentration increased, the K_m value decreased and the V_{max} increased, thereby elevating the CL_{int}. The CL_{int} in the presence of 40 μM gefitinib was 2.8 times higher than that in the absence of the gefitinib.

These findings indicated that similar results were obtained with human liver microsomes and human small intestinal microsomes. With both systems, gefitinib had opposing effects on the formation of NPC and that of APC from irinotecan by CYP3A4. Gefitinib inhibited the formation of NPC but stimulated the formation of APC.

Effects of Gefitinib on Midazolam 1′-Hydroxylase Activity of CYP3A in Human Liver Microsomes. We examined whether gefitinib stimulated the metabolism of other CYP3A substrates. Midazolam is a representative substrate of human CYP3A. It is efficiently metabolized to 1′-hydroxymidazolam by human CYP3A. The effects of gefitinib on midazolam 1′-hydroxylase activity were examined with the use of human liver microsomes. The results are shown in Table 4. The addition of 10 μM gefitinib to the reaction mixture increased midazolam 1′-hydroxylase activity to 304% as compared with control. The substrate α-naphthoflavone also increased midazolam 1′-hydroxylation catalyzed by CYP3A, consistent with the results of Maenpaa et al. (1998).

Discussion

This study was designed to test the hypothesis that gefitinib, a substrate of CYP3A, increases the bioavailability of irinotecan by inhibiting drug metabolism, as proposed by Stewart et al. (2004). We had initially anticipated that gefitinib would inhibit the CYP3A4-mediated formation of both NPC and APC. As shown in Figs. 2 and 3, NPC formation was inhibited by gefitinib as expected. However, APC formation was stimulated by the addition of gefitinib. In the liver microsomes, CL_{int} values for NPC and APC formation were 2.9 and 0.68 μl/min/mg protein, respectively (Table 2), indicating that NPC formation was the major pathway for irinotecan metabolism by CYP3A4. The effects of gefitinib on CL_{int} for NPC formation were higher than those on CL_{int} for APC. Therefore, total metabolic clearance decreased according to the increase of gefitinib concentration. The NPC formation was also the major pathway for irinotecan metabolism by CYP3A4 in the intestinal microsomes (Table 3). However, total metabolic clearance was not necessarily decreased by the addition of gefitinib, since the effects of gefitinib on CL_{int} values for NPC and APC formation depended on the gefitinib concentrations. The effects of gefitinib on the bioavailability of orally administered irinotecan thus cannot be simply explained by our findings. Our results suggest that gefitinib-induced inhibition of mouse CYP3A enzymes present in the liver and the small intestine might not be responsible for the increase in the bioavailability of orally adminis-

TABLE 2

The effects of gefitinib on the apparent kinetic parameters for NPC and APC formation by CYP3A4 in human liver microsomes

Gefitinib	NPC Formation			APC Formation		
	K_m	V_{max}	CL_{int}	K_m	V_{max}	CL_{int}
	μM	*pmol/min/mg protein*	*μl/min/mg protein*	*μM*	*pmol/min/mg protein*	*μl/min/mg protein*
0 μM	44	128	2.9	68	46	0.68
5 μM	48	85	1.8	47	45	0.96
10 μM	46	73	1.6	54	61	1.1
20 μM	49	58	1.2	51	64	1.3
40 μM	93	69	0.74	159	153	0.96

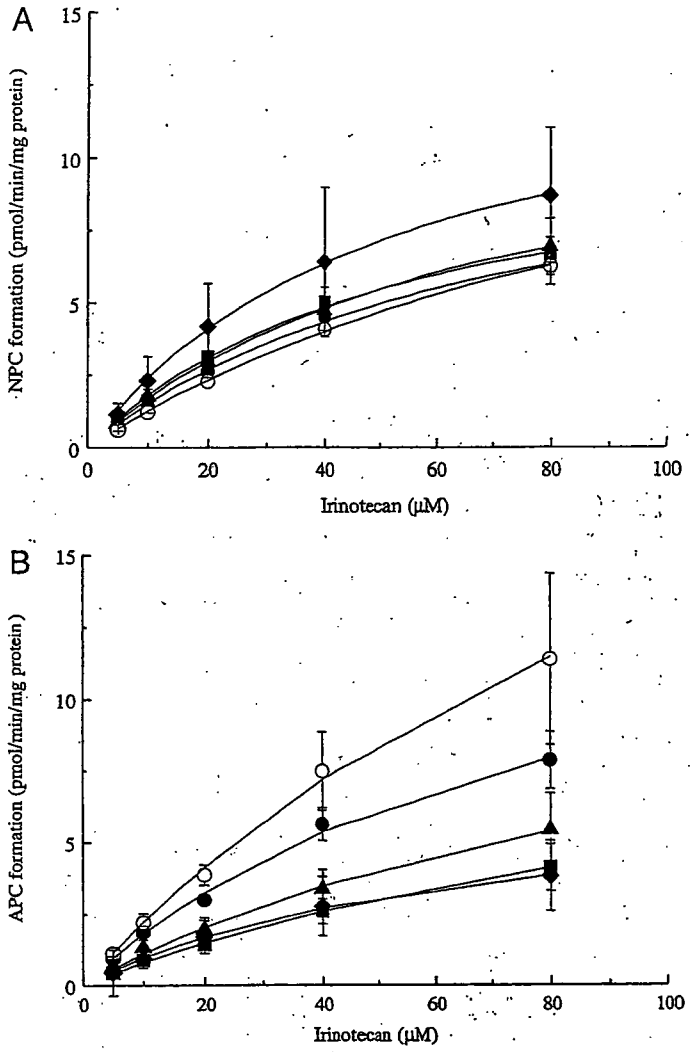

FIG. 3. Velocity versus substrate concentration plots for irinotecan metabolism by CYP3A4 in human small intestinal microsomes. A, NPC formation; B, APC formation. Each data point represents the mean of triplicate determinations and is shown with standard deviation bars. ◇, 0 μM gefitinib; ■, 5 μM gefitinib; ▲, 10 μM gefitinib; ●, 20 μM gefitinib; ○, 40 μM gefitinib.

tered irinotecan and the subsequent rise in the plasma concentration of SN-38 as reported by Stewart et al. (2004).

In humans, the concentration of SN-38 in plasma is associated not only with the response to irinotecan, but also with the dose-limiting toxicity of irinotecan, such as leukopenia, diarrhea, or both (Negoro et al., 1991; Akabayashi, 1997). Severe, occasionally fatal toxicity occurs sporadically, even in low-risk patients participating in well controlled clinical trials (Negoro et al., 1991; Kudoh et al., 1998; Rougier et al., 1998). Thus, the risk of drug interactions further increasing the plasma concentration of SN-38 merits close examination. The plasma SN-38 concentration is affected by the metabolism of irinotecan by carboxylesterases to form SN-38 as well as by the metabolism of irinotecan by CYP3A4 to form NPC and APC. The SN-38 concentration is also influenced by glucuronidation catalyzed by UDP-glucuronosyltransferase 1A1 (detoxification) and by bile excretion by ABCC2 transporter (Mathijssen et al., 2003). Any of these processes may be affected, leading to drug interactions. Our study focused on the effects of gefitinib on the CYP3A4-mediated metabolism of irinotecan. Our results showed that gefitinib had different effects on the formation of NPC and that of APC from irinotecan, making it difficult to predict changes in the plasma SN-38 concentration caused by gefitinib-induced alteration of CYP3A4-catalyzed metabolism. An understanding of the full picture of drug interactions between irinotecan and gefitinib thus requires consideration of the effects of gefitinib on other pharmacokinetic processes of irinotecan.

Gefitinib-induced inhibition of NPC formation and activation of APC formation from irinotecan occurred at concentrations of 5 μM or higher. The daily oral administration of gefitinib at recommended doses results in mean steady-state plasma concentrations ranging from 0.4 to 1.4 μM (Albanell et al., 2002). However, the local concentration of gefitinib in enterocytes immediately after oral administration is probably much higher than the plasma concentration. Therefore, if irinotecan and gefitinib are simultaneously administered, gefitinib present in enterocytes may affect the CYP3A4-mediated metabolism of irinotecan in the small intestine.

A progressive decrease in V_{max} for NPC formation was induced by the addition of gefitinib in human liver microsomes (Table 2), whereas no effects were seen when human small intestinal microsomes were used (Table 3). These results suggest that differences in tissue from which CYP3A4 expresses may affect the enzymatic properties of CYP3A4. In the case of APC formation, progressive increases in V_{max} values were observed by the addition of gefitinib in both microsomes, indicating the activation of the metabolism. However, K_m values were somewhat random. At present, the reason is unclear.

CYP3A4 is a complex heme-containing enzyme that exhibits homotropic and heterotropic cooperativity toward several substrates (Hutzler and Tracy, 2002). For example, α-naphthoflavone shows activation kinetics toward CYP3A-mediated metabolism depending on the heterotropic positive cooperativity to substrates such as aflatoxin B, progesterone, and phenanthrene (Schwab et al., 1988; Shou et al., 1994; Ueng et al., 1997). Previous studies have suggested that CYP3A4 has a noncatalytic effector site within the active-site cavity, capable of modulating its function (Shou et al., 1994). Similar to the results seen in the present study, pathway differential effects on CYP3A4-mediated metabolism of midazolam and triazolam by testosterone have been reported (Schrag and Wienkers, 2001; Galetin et al., 2003). Galetin et al. (2002) have also shown the similar effects of quinidine on the metabolism of midazolam by CYP3A4. Taking these results into account, the pathway differential effects of a certain effector on the metabolism of a chemical, which is

TABLE 3

The effects of gefitinib on the apparent kinetic parameters for NPC and APC formation by CYP3A4 in human small intestinal microsomes

Gefitinib	NPC Formation			APC Formation		
	K_m	V_{max}	CL_{int}	K_m	V_{max}	CL_{int}
	μM	*pmol/min/mg protein*	*μl/min/mg protein*	*μM*	*pmol/min/mg protein*	*μl/min/mg protein*
0 μM	49	15	0.31	59	6.7	0.11
5 μM	52	11	0.21	114	9.9	0.087
10 μM	64	12	0.19	97	12	0.12
20 μM	67	11	0.16	73	15	0.21
40 μM	106	15	0.14	91	28	0.31

TABLE 4

Effects of gefitinib on midazolam 1′-hydroxylase activity of CYP3A in human liver microsomes

The concentration of midazolam was 10 μM. The control activity of midazolam 1′-hydroxylase activity determined in the absence of an effecter was 0.408 nmol/min/mg protein.

Chemical	Concentration	1′-Hydroxymidazolam Formation[a]
	μM	*% of control*
Gefitinib	5.0	221 ± 4.5[b]
	10.0	304 ± 5.3[b]
α-Naphthoflavone	5.0	189 ± 1.2[b]
	10.0	212 ± 7.5[b]

[a] Values are represented as mean ± S.D. (n = 3).
[b] Significant difference between values obtained in the presence or absence of an activator ($P < 0.05$).

simultaneously metabolized by CYP3A4 to form multiple metabolites, might be general mechanisms of CYP3A4 enzyme. The crystal structure of CYP3A4, directly supporting the presence of multiple substrate-binding active sites on CYP3A4 enzyme (Williams et al., 2004), may provide a clue to clarify the mechanisms.

We examined the effects of α-naphthoflavone in combination with gefitinib on the CYP3A4-mediated NPC formation. A 5 μM concentration of α-naphthoflavone and 40 μM gefitinib were simultaneously added to a reaction mixture containing 20 μM irinotecan and liver microsomes. These concentrations used were the same as those shown in Table 1. The addition of α-naphthoflavone did not alter the inhibitory effects of gefitinib on NPC formation (data not shown).

Gefitinib stimulated not only APC formation from irinotecan, but also midazolam 1′-hydroxylation catalyzed by CYP3A (Table 4). Gefitinib might also stimulate the metabolism of other CYP3A substrates in the liver and small intestine, thereby reducing drug bioavailability. Steroids such as dexamethasone (Gentile et al., 1996) and antiemetic agents such as ondansetron (Villikka et al., 1999), which are also metabolized by CYP3A4, are usually coadministered with gefitinib in patients who require chemotherapy. Whether gefitinib alters the pharmacokinetics (metabolic clearance) and the pharmacodynamic effects of these drugs should be clarified in vivo.

In the present study, the 4′-hydroxymidazolam formation was detectable with the HPLC analysis used. However, unfortunately, the 4′-hydroxymidazolam was not quantified in the presence of gefitinib, since a peak derived from gefitinib or its metabolite disturbed the detection of the 4′-hydroxymidazolam.

In conclusion, our in vitro studies demonstrated that gefitinib had opposing effects on the CYP3A4-catalyzed formation of NPC and that of APC from irinotecan, i.e., gefitinib inhibited the formation of NPC but stimulated the formation of APC.

References

Akabayashi A (1997) Questions raised over release of side-effects data in Japan. *Lancet* **350**:124.

Albanell J, Rojo F, Averbuch S, Feyereislova A, Mascaro JM, Herbst R, LoRusso P, Rischin D, Sauleda S, Gee J, et al. (2002) Pharmacodynamic studies of the epidermal growth factor receptor inhibitor ZD1839 in skin from cancer patients: histopathologic and molecular consequences of receptor inhibition. *J Clin Oncol* **20**:110–124.

Barker AJ, Gibson KH, Grundy W, Godfrey AA, Barlow JJ, Healy MP, Woodburn JR, Ashton SE, Curry BJ, Scarlett L, et al. (2001) Studies leading to the identification of ZD1839 (IRESSA): an orally active, selective epidermal growth factor receptor tyrosine kinase inhibitor targeted to the treatment of cancer. *Bioorg Med Chem Lett* **11**:1911–1914.

Cohen MH, Williams GA, Sridhara R, Chen G, McGuinn WD Jr, Morse D, Abraham S, Rahman A, Liang C, Lostritto R, et al. (2004) United States Food and Drug Administration drug approval summary: gefitinib (ZD1839; Iressa) tablets. *Clin Cancer Res* **10**:1212–1218.

Culy CR and Faulds D (2002) Gefitinib. *Drugs* **62**:2237–2248.

Fujita K, Hidaka M, Takamura N, Yamasaki K, Iwakiri T, Okumura M, Kodama H, Yamaguchi M, Ikenoue T, and Arimori K (2003) Inhibitory effects of citrus fruits on cytochrome P450 3A (CYP3A) activity in humans. *Biol Pharm Bull* **26**:1371–1373.

Galetin A, Clarke SE, and Houston JB (2002) Quinidine and haloperidol as modifiers of CYP3A4 activity: multisite kinetic model approach. *Drug Metab Dispos* **30**:1512–1522.

Galetin A, Clarke SE, and Houston JB (2003) Multisite kinetic analysis of interactions between prototypical CYP3A4 subgroup substrates: midazolam, testosterone and nifedipine. *Drug Metab Dispos* **31**:1108–1116.

Gentile DM, Tomlinson ES, Maggs JL, Park BK, and Back DJ (1996) Dexamethasone metabolism by human liver in vitro. Metabolite identification and inhibition of 6-hydroxylation. *J Pharmacol Exp Ther* **277**:105–112.

Haaz MC, Riche C, Rivory LP, and Robert J (1998a) Biosynthesis of an aminopiperidino metabolite of irinotecan [7-ethyl-10-[4-(1-piperidino)-1-piperidino]carbonyloxycamptothecine] by human hepatic microsomes. *Drug Metab Dispos* **26**:769–774.

Haaz MC, Rivory L, Riche C, Vernillet L, and Robert J (1998b) Metabolism of irinotecan (CPT-11) by human hepatic microsomes: participation of cytochrome P-450 3A and drug interactions. *Cancer Res* **58**:468–472.

Harlow GR and Halpert JR (1997) Alanine-scanning mutagenesis of a putative substrate recognition site in human cytochrome P450 3A4. Role of residues 210 and 211 in flavonoid activation and substrate specificity. *J Biol Chem* **272**:5396–5402.

Honig PK, Wortham C, Hull R, Zamani K, Smith JE, and Cantilena LR (1993a) Itraconazol affects single-dose terfenadine pharmacokinetics and cardiac repolarization pharmacodynamics. *J Clin Pharmacol* **33**:1201–1206.

Honig PK, Wortham C, Zamani K, Conner DP, Mullin JC, and Cantilena LR (1993b) Terfenadine-ketoconazole interaction: pharmacokinetic and electrocardiographic consequences. *J Am Med Assoc* **269**:1513–1518.

Honig PK, Wortham C, Zamani K, Mullin JC, Conner DP, and Cantilena LR (1993c) The effect of fluconazole on the steady-state pharmacokinetics and electrocardiographic pharmacodynamics of terfenadine in humans. *Clin Pharmacol Ther* **53**:630–636.

Hutzler JM and Tracy TS (2002) Atypical kinetic profiles in drug metabolism reactions. *Drug Metab Dispos* **30**:355–362.

Koley AP, Buters JT, Robinson RC, Markowitz A, and Friedman FK (1997) Differential mechanisms of cytochrome P450 inhibition and activation by alpha-naphthoflavone. *J Biol Chem* **272**:3149–3152.

Kudoh S, Fujiwara Y, Takada Y, Yamamoto H, Kinoshita A, Ariyoshi Y, Furuse K, and Fukuoka M (1998) Phase II study of irinotecan combined with cisplatin in patients with previously untreated small-cell lung cancer. *J Clin Oncol* **16**:1068–1074.

Kuppens IE, Beijnen J, and Schellens JH (2004) Topoisomerase I inhibitors in the treatment of gastrointestinal cancer: from intravenous to oral administration. Topoisomerase I inhibitors in the treatment of gastrointestinal cancer: from intravenous to oral administration. *Clin Colorectal Cancer* **4**:163–180.

Maenpaa J, Hall SD, Ring BJ, Strom SC, and Wrighton SA (1998) Human cytochrome P450 3A (CYP3A) mediated midazolam metabolism: the effect of assay conditions and regioselective stimulation by alpha-naphthoflavone, terfenadine and testosterone. *Pharmacogenetics* **8**:137–155.

Mathijssen RH, de Jong FA, and van Schaik RH (2004) Prediction of irinotecan pharmacokinetics by use of cytochrome P450 3A4 phenotyping probes. *J Natl Cancer Inst* **96**:1585–1592.

Mathijssen RH, Marsh S, Karlsson MO, Xie R, Baker SD, Verweij J, Sparreboom A, and McLeod HL (2003) Irinotecan pathway genotype analysis to predict pharmacokinetics. *Clin Cancer Res* **9**:3246–3253.

McKillop D, McCormick AD, Millar A, Miles GS, Phillips PJ, and Hutchison M (2005) Cytochrome P450-dependent metabolism of gefitinib. *Xenobiotica* **35**:39–50.

Negoro S, Fukuoka M, Masuda N, Takada M, Kusunoki Y, Matsui K, Takifuji N, Kudoh S, Niitani H, and Taguchi T (1991) Phase I study of weekly intravenous infusion of CPT-11, a new derivative of camptothecin, in the treatment of advanced non-small-cell lung cancer. *J Natl Cancer Inst* **83**:1164–1168.

Nelson DR, Koymans L, Kamataki T, Stegeman JJ, Feyereisen R, Waxman DJ, Waterman MR, Gotoh O, Coon MJ, Estabrook RW, et al. (1996) P450 superfamily: update on new sequences, gene mapping, accession numbers and nomenclature. *Pharmacogenetics* **6**:1–42.

Rougier P, Van Cutsem E, Bajetta E, Niederle N, Possinger K, Labianca R, Navarro M, Morant R, Bleiberg H, Wils J, et al. (1998) Randomised trial of irinotecan *versus* fluorouracil by continuous infusion after fluorouracil failure in patients with metastatic colorectal cancer. *Lancet* **352**:1407–1412.

Sakuma T, Takai M, Endo Y, Kuroiwa M, Ohara A, Jarukamjorn K, Honma R, and Nemoto N (2000) A novel female-specific member of the CYP3A gene subfamily in the mouse liver. *Arch Biochem Biophys* **377**:153–162.

Santos A, Zanetta S, Cresteil T, Deroussent A, Pein F, Raymond E, Vernillet L, Risse ML, Boige V, Gouyette A, et al. (2000) Metabolism of irinotecan (CPT-11) by CYP3A4 and CYP3A5 in humans. *Clin Cancer Res* **6**:2012–2020.

Schrag ML and Wienkers LC (2001) Triazolam substrate inhibition: evidence of competition for heme-bound reactive oxygen within the CYP3A4 active site. *Drug Metab Dispos* **29**:70–75.

Schwab GE, Raucy JL, and Johnson EF (1988) Modulation of rabbit and human hepatic cytochrome P-450-catalyzed steroid hydroxylations by alpha-naphthoflavone. *Mol Pharmacol* **33**:493–499.

Shou M, Grogan J, Mancewicz JA, Krausz KW, Gonzalez FJ, Gelboin HV, and Korzekwa KR (1994) Activation of CYP3A4: evidence for the simultaneous binding of two substrates in a cytochrome P450 active site. *Biochemistry* **33**:6450–6455.

Stewart CF, Leggas M, Schuetz JD, Panetta JC, Cheshire PJ, Peterson J, Daw N, Jenkins JJ 3rd, Gilbertson R, Germain GS, et al. (2004) Gefitinib enhances the antitumor activity and oral bioavailability of irinotecan in mice. *Cancer Res* **64**:7491–7499.

Ueng YF, Kuwabara T, Chun YJ, and Guengerich FP (1997) Cooperativity in oxidations catalyzed by cytochrome P450 3A4. *Biochemistry* **36**:370–381.

Villikka K, Kivisto KT, and Neuvonen PJ (1999) The effect of rifampin on the pharmacokinetics of oral and intravenous ondansetron. *Clin Pharmacol Ther* **65**:377–381.

Ward WH, Cook PN, Slater AM, Davies DH, Holdgate GA, and Green LR (1994) Epidermal growth factor receptor tyrosine kinase. Investigation of catalytic mechanism, structure-based searching and discovery of a potent inhibitor. *Biochem Pharmacol* **48**:659–666.

Williams PA, Cosme J, Vinkovic DM, Ward A, Angove HC, Day PJ, Vonrhein C, Tickle IJ, and Jhoti H (2004) Crystal structures of human cytochrome P450 3A4 bound to metyrapone and progesterone. *Science (Wash DC)* **305**:683–686.

Zhang QY, Dunbar D, and Kaminsky LS (2003) Characterization of mouse small intestinal cytochrome P450 expression. *Drug Metab Dispos* **31**:1346–1351.

Address correspondence to: Dr. Ken-ichi Fujita, Department of Clinical Oncology, Saitama Medical School, 38 Morohongou, Moroyama-cho, Iruma-gun, Saitama, 350-0495, Japan. E-mail: fujitak@saitama-med.ac.jp

CASE REPORT

Radiation Medicine, Vol. 23 No. 5, 371–375 p.p., 2005

Hepatic Hemangioma Presenting Atypical Radiologic Findings: A Case Report

Ayu Hosokawa,* Tetsuo Maeda,* Ukihide Tateishi,* Mitsuo Satake,* Ryoko Iwata,* Hidenori Ojima,** and Yasuaki Arai*

A 69-year-old woman was referred to our hospital due to a liver tumor that was incidentally noted on ultrasound (US). US revealed a pedunculated mass of 5 cm in diameter, with a heterogeneous echo pattern. On arterial phase dynamic contrast-enhanced computed tomography (CT), a tiny enhancing dot in the upper aspect of the mass was seen; whereas, the main portion of the lesion appeared as hypoattenuating. The tumor was of low intensity on T1-weighted magnetic resonance (MR) images, and showed slightly heterogeneous high intensity on T2-weighted MR images. The most characteristic feature of the tumor was its exophytic appearance. On post-gadolinium hepatic arterial dominant-phase MR images, the tumor showed nodular enhancement centrally, with progressive spread of enhancement on later images. Angiography showed dilatation of the right posterior inferior branch of the hepatic artery and C-shaped opacification. Since we could not rule out malignancy for these nonspecific radiologic findings, a partial resection of the liver was carried out, resulting in a pathological diagnosis of hepatic hemangioma. This hemangioma had marked hyalinization and fibrosis, causing a heterogeneous appearance on MR images. The tumor presented an exophytic appearance, which caused some diagnostic confusion.

Key words: hepatic hemangioma, exophytic appearance, hyalinization

Introduction

Hemangioma, the most common benign hepatic tumor, is frequently incidentally detected by ultrasound (US) and computed tomography (CT) in asymptomatic patients. It is therefore important to distinguish hemangioma from other hepatic neoplasms. In cases of typical hemangioma with characteristic findings, imaging modalities are highly reliable for diagnosis. However, there are a few atypical hemangiomas that may cause difficulties for radiologic diagnosis. We report the case of an atypical hepatic hemangioma presenting an exophytic appearance mimicking hepatic malignancy.

Received September 3, 2004; revision accepted January 4, 2005.

*Division of Diagnostic Radiology, National Cancer Center Hospital

**Division of Pathology, National Cancer Center Research Institute

Reprint requests to Ayu Hosokawa, M.D., Division of Diagnostic Radiology, National Cancer Center Hospital, 5-1-1 Tsukiji, Chuo-ku, Tokyo 104-0045, JAPAN.

Case Report

A 69-year-old woman was referred to our hospital due to a liver tumor that was incidentally pointed out by US. On physical examination, the abdominal mass was not palpable. Liver function studies were normal. Serum levels of carcinoembryonic antigen, α-fetoprotein, and PIVKA-II were all within normal ranges. Hepatitis B surface antigen and hepatitis C antibody were negative.

US revealed a 5 cm pedunculated mass with heterogeneous echo pattern. Nonenhanced CT scan showed the exophytic mass in the right posterior inferior portion of the liver. After intravenous administration of contrast material, the arterial-phase CT showed minimal and no enhancement except for a tiny enhancing dot in the anterior aspect of the mass. Although the delayed-phase CT indicated more than half of the mass showing slight enhancement, the mass appeared hypoattenuating relative to the normal liver parenchyma (Fig. 1).

The tumor was of low intensity on T1-weighted MR images, and was moderately hyperintense on T2-weighted MR images. Hepatic arterial-dominant phase post-gadolinium MR images showed nodular enhance-

Fig. 1.
A: Nonenhanced CT scan shows an exophytic mass of 5 cm in diameter in the right posterior inferior portion of the liver (*arrows*), and the liver parenchyma (*arrowheads*).
B: After intravenous administration of contrast material, arterial-phase CT shows a tiny enhancing dot (*arrow*) isoattenuating to aortic enhancement.
C: The main part of the tumor (*arrows*) shows heterogeneous enhancement hypoattenuating compared to that of liver parenchyma (*arrowheads*) on delayed images.

A | B | C

ment centrally, with progressive enhancement on delayed images (Fig. 2).

Hepatic angiogram showed dilatation of the right posterior inferior branch of the hepatic artery and C-shaped opacification (Fig. 3).

Since we could not rule out malignant tumor based on these radiologic findings, partial resection of the liver was carried out. At surgery, a round tumor with capsule was seen, but no adhesion or peritoneal fluid was noted. The tumor was pedunculated and connected to the liver (subsegment 6) by a stalk of 3 cm in length. Macroscopically, the tumor measured 6.0×5.5×4.5 cm and was whitish, elastic, slightly firm, and well demarcated from the surrounding liver parenchyma. The cut surface of the tumor showed a whitish hyalinized area with dark red patches centrally and a tan-to-yellowish area peripherally (Fig. 4A). Histologically, there were multiple vessels of various sizes with marked hyaline-like degeneration in the central area, whereas small-sized vessels with rich fibrous stroma were predominant in the peripheral area (Figs. 4B, C). Somewhat large venous and arterial branches and large lymph vessels were seen in the border between the tumor and liver parenchyma. A pathological diagnosis of hepatic hemangioma was made.

The postoperative course was uneventful, and the patient was discharged 10 days after surgery.

Discussion

Hemangioma is the most common benign tumor of the liver. The incidence of hemangioma in the general population varies in published reports from 0.4% to 20%.[1]

The typical radiologic features of cavernous hemangiomas have been well described, and it is usually easy to differentiate hemangioma from other liver tumors. However, the present case had atypical radiologic features, which caused some diagnostic confusion.

The typical US appearance is that of a homogeneous, hyperechoic mass with well-defined margins and some posterior echo enhancement.[2] In contrast to these features, in the present case, the internal echo pattern was partially hypoechoic and heterogeneous.

Strict criteria for the classic CT appearance of hepatic hemangioma include: relative hypoattenuation compared with normal liver on precontrast images, early peripheral enhancement, progressive spread of the opacified area towards the center of the lesion, and complete isoattenuating fill-in occurring not less than 3 minutes nor more than 60 minutes after contrast material administration.[3] Although the present tumor had a tiny enhancing dot in the arterial phase, early peripheral enhancement and progressive opacification towards the center of the lesion was not clear.

Hemangioma typically demonstrates marked high intensity on T2-weighted MR images and is usually spheroid or ovoid (87%).[3,4] However, the present tumor showed a moderately hyperintense and heterogeneous appearance on T2-weighted MR images.

In the present case, the hepatic angiogram showed dilatation of the right posterior inferior branch of the

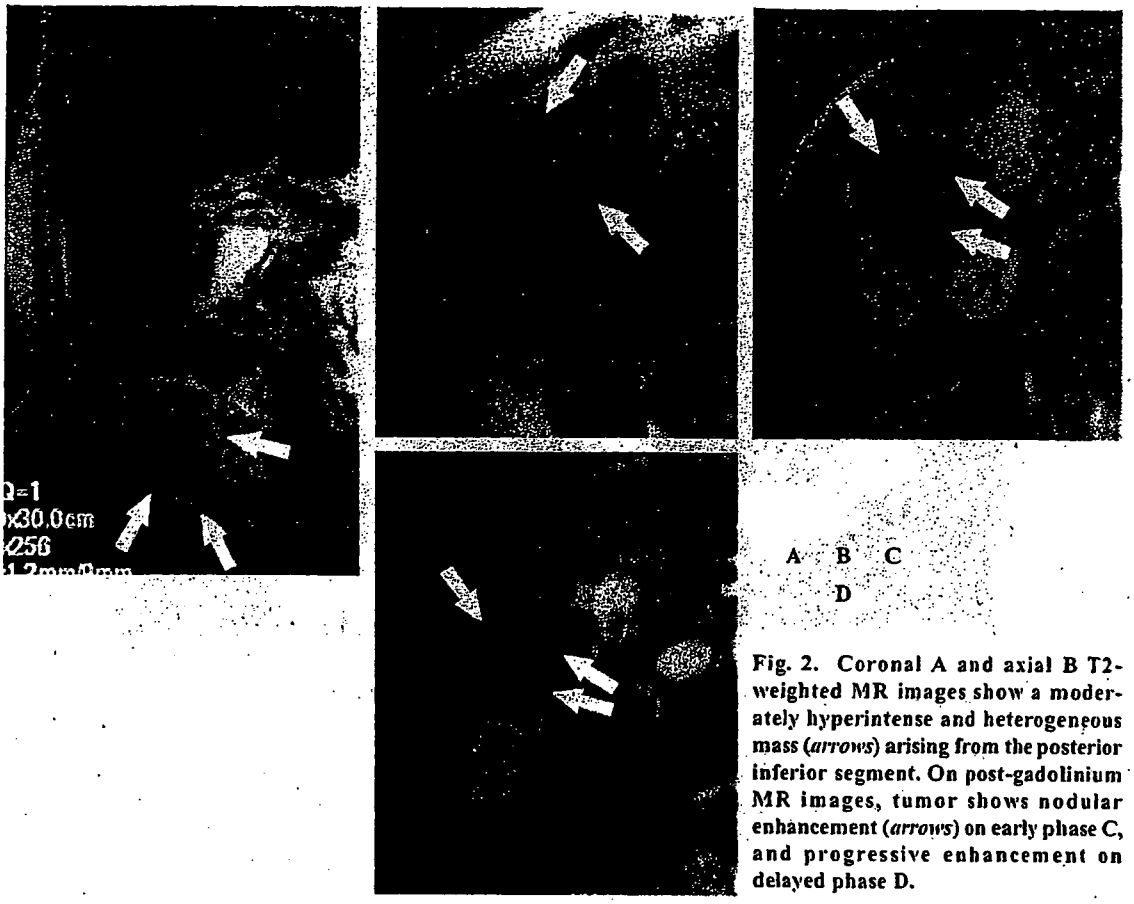

Fig. 2. Coronal A and axial B T2-weighted MR images show a moderately hyperintense and heterogeneous mass (*arrows*) arising from the posterior inferior segment. On post-gadolinium MR images, tumor shows nodular enhancement (*arrows*) on early phase C, and progressive enhancement on delayed phase D.

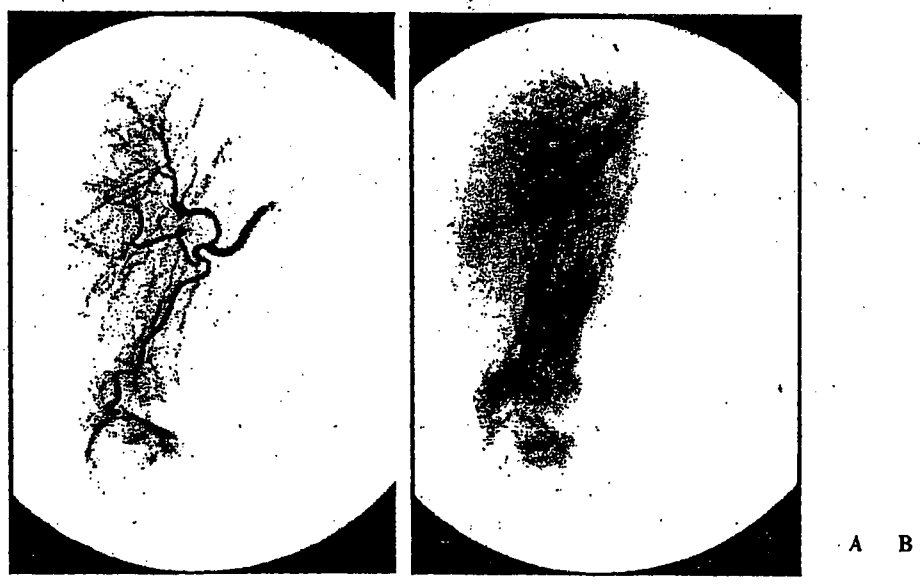

Fig. 3.
A: Selective hepatic angiogram shows dilatation of the right posterior inferior branch of the hepatic artery and C-shaped opacification.
B: Venous phase of hepatic angiogram shows mildly persistent peripheral enhancement.

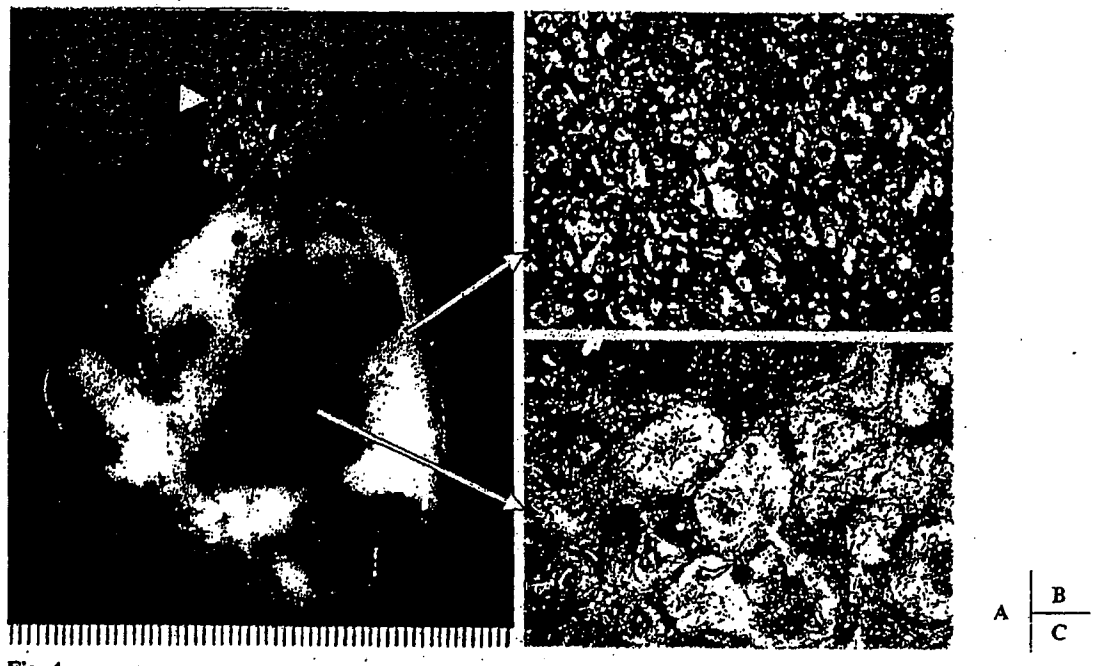

Fig. 4.
A: The resected tumor is a 6.0×5.5×4.5 cm mass with a 3-cm-long stalk. The cut surface of the tumor shows the whitish hyalinized area with dark red patches centrally and the tan-to-yellowish area peripherally. The stalk is seen (*arrowhead*).
B: The peripheral area of the tumor shows small-sized vessels with rich fibrous stroma.
C: The central area shows multiple vessels of various sizes with marked hyaline-like degeneration (Hematoxylin-eosin stain, original magnification ×40).

hepatic artery. Despite dilated feeding vessels, tumor vessels or vascular enhancement were not recognized. Dilated and tortuous feeding arteries are generally rare in hepatic hemangioma.[5]

The present tumor demonstrated radiologic findings inconsistent with those of typical hemangioma in all modalities. Nevertheless, this tumor showed a tiny enhancing dot in the arterial-phase CT scan that was considered to be consistent with the "bright dot" sign. Jang *et al.* advocated that this sign could be helpful in diagnosing small hemangiomas with nonspecific hypoattenuation at the arterial phase and portal venous phase of spiral CT.[6] In our case, there might have been a chance of a correct diagnosis preoperatively. However, the "bright dot" sign is characteristic of small hemangiomas (<2 cm in diameter), and it is uncertain whether this sign is reliable for large hemangiomas like our case (>4 cm in diameter). Further experience is needed.

The surgical procedure for benign hepatic tumors has been controversial. Terkivatan *et al.* reported that they advised surgery for any benign hepatic tumor that caused severe complaints and when there was an uncertain diagnosis.[7] In the present case, since the patient was asymptomatic, a radiologic follow-up or percutaneous needle biopsy might have been a reasonable option. However, we selected resection for the uncertain hepatic tumor because of its relatively large diameter, risk of rupture of the exophytic lesion, and the inability to exclude malignancy.

Histopathologically, multiple vessels of various sizes, remarkable hyalinization, and fibrosis of the stroma were present without a cavernous pattern in our case. The pathological diagnosis of hemangioma was based on the presence of variably sized, endothelial-lined vascular channels.

We considered various reasons for these atypical radiologic features. First, remarkable hyalinization and fibrosis without a cavernous pattern of the tumor can be causative of minimal enhancement. Some investigators reported that the reasons for nonenhancement of hemangioma were slow flow in the central sinusoids, central fibrosis, central thrombosis, and hemorrhage.[5,8] Yamashita *et al.* advocated that enhancement patterns and hemodynamic characteristics of hemangiomas could vary depending on the internal architecture of the lesion.[9] Second, the current tumor presented an exophytic appearance. According to Brancatelli *et al.*, 12% of hemangiomas demonstrate exophytic growth.[1] Moreover, pedunculated hemangiomas are very rare.[10] Third, the relatively large size of the present tumor could have

been the reason for atypical radiologic findings. Hepatic hemangiomas are typically less than 3 cm in diameter. When larger than 4 cm, Nelson *et al.* classified them as "giant hemangioma".[3] Generally, on dynamic contrast-enhanced CT scans, delayed imaging of large hemangioma shows further centripetal enhancement, however, complete filling with contrast material has never been observed.[11] Large hemangioma has a spectrum of histopathologic changes, including hemorrhage, thrombosis, extensive hyalinization, liquefaction, and fibrosis.[5,8,11] These features cause a heterogeneous appearance on MR images. There occasionally exists confusion in distinction between giant hemangioma and malignant tumors including necrotic metastatic tumor and hepatocellular carcinoma.[11] In fact, although the present tumor had no cystic degeneration, it was difficult to exclude those malignant hepatic tumors beforehand. Furthermore, primary hepatic angiosarcoma should be added to the differential diagnosis when dynamic CT and MR imaging show heterogeneous enhancement on early-phase images and progressive enhancement on delayed images.[12]

Some authors have suggested that hyalinized hemangiomas represent an end stage of hemangioma involution.[13] This case might therefore be regarded as an incomplete stage to hyalinization.

In summary, our report documents an unusual radiologic manifestation of hepatic hemangioma. Hemangioma should be considered in the differential diagnosis when a tumor shows a large heterogeneous mass with a tiny enhancing dot, even if the tumor is pedunculated.

References

1) Brancatelli G, Federle MP, Blachar A, Grazioli L. Hemangioma in the cirrhotic liver: diagnosis and natural history. *Radiology*, 219: 69–74, 2001.
2) Moody AR, Wilson SR. Atypical hepatic hemangioma: a suggestive sonographic morphology. *Radiology*, 188: 413–417, 1993.
3) Nelson RC, Chezmar JL. Diagnostic approach to hepatic hemangiomas. *Radiology*, 176: 11–13, 1990.
4) Tung GA, Vaccaro JP, Cronan JJ, Rogg JM. Cavernous hemangioma of the liver: pathologic correlation with high-field MR imaging. *AJR Am J Roentgenol*, 162: 1113–1117, 1994.
5) Takayasu K, Moriyama N, Shima Y, *et al.* Atypical radiographic findings in hepatic cavernous hemagioma: correlation with histologic features. *AJR Am J Roentgenol*, 146: 1149–1153, 1986
6) Jang HJ, Choi BI, Kim TK, *et al.* Atypical small hemangiomas of the liver: "bright dot" sign at two-phase spiral CT. *Radiology*, 208: 543–548, 1998.
7) Terkivatan T, de Wilt JH, de Man RA, *et al.* Indications and long-term outcome of treatment for benign hepatic tumors: a critical appraisal. *Arch Surg*, 136: 1033–1038, 2001.
8) Johnson CM, Sheedy PF 2nd, Stanson AW, Stephens DH, Hattery RR, Adson MA. Computed tomography and angiography of cavernous hemangiomas of the liver. *Radiology*, 138: 115–121, 1981.
9) Yamashita Y, Ogata I, Urata J, Takahashi M. Cavernous hemangioma of the liver: pathologic correlation with dynamic CT fingings. *Radiology*, 203: 121–125, 1997.
10) Bader TR, Braga L, Semelka RC. Exophytic benign tumors of the liver: appearance on MRI. *Magn Reson Imaging*, 19: 623–628, 2001.
11) Choi BI, Han MC, Park JH, Kim SH, Han MH, Kim CW. Giant cavernous hemangioma of the liver: CT and MR imaging in 10 cases. *AJR Am J Roentgenol*, 152: 1221–1226, 1989.
12) Koyama T, Fletcher JG, Johnson CD, Kuo MS, Notohara K, Burgart LJ. Primary hepatic angiosarcoma: findings at CT and MR imaging. *Radiology*, 222: 667–673, 2002.
13) Vilgrain V, Boulos L, Vullierme MP, Denys A, Terris B, Menu Y. Imaging of atypical hemangiomas of the liver with pathologic correlation. *Radiographics*, 20: 379–397, 2000.

Prediction of Lung Adenocarcinoma Without Vessel Invasion*

A CT Scan Volumetric Analysis

Ukihide Tateishi, MD, PhD; Hajime Uno, PhD; Kari Yonemori, MD; Mistuo Satake, MD; Masahiro Takeuchi, ScD, MPH; and Yasuaki Arai, MD, PhD

Study objectives: **Patients with lung adenocarcinoma without vessel invasion have a favorable prognosis after resection and are among the candidates for limited surgery. The purpose of the present study was to predict lung adenocarcinoma without vessel invasion based on a volumetric analysis of the lesion with a CT scan prior to the operation.**

Methods: **CT scan images were obtained in 288 consecutive patients with adenocarcinoma of the lung before surgical resection. Total tumor volume, the volume of the nonsolid component, and the proportion occupied by the nonsolid component were calculated by the perimeter method. The performance of the derived logistic regression model and the volumetric results were evaluated by receiver operating characteristic analysis. The model derived for the prediction of tumors without vessel invasion was assessed by means of the leave-one-out cross-validation technique.**

Results: **The pathologic diagnosis was adenocarcinoma with vessel invasion in 160 cases, and without vessel invasion in 128 cases. The median total tumor volume, the median volume of the nonsolid component, and median proportion occupied by the nonsolid component were 1,123.7 mm^3, 253.4 mm^3, and 58.0%, respectively. With the derivation of the predictive rule, stepwise regression yielded the following five features: the proportion occupied by the nonsolid component; spiculation; pleural indentation; gender; and tumor size. The Az value, a measure of diagnostic power represented as the area under the curve, was 0.957 for prediction of lung adenocarcinoma without vessel invasion. The cross-validation accuracy achieved by applying the rule was 90.3%.**

Conclusions: **The proportion occupied by the nonsolid component based on a CT scan volumetric analysis was a reliable predictor of tumors without vessel invasion in patients with adenocarcinoma of the lung.** *(CHEST 2005; 128:3276–3283)*

Key words: CT scan; lung; lung cancer

Abbreviations: CI = confidence interval; OR = odds ratio; ROC = receiver operating characteristic; SPN = solitary pulmonary nodule

Patients with lung adenocarcinoma without vessel invasion clearly have the best outcome after resection, and they are among the candidates for limited surgery.[1,2] Some studies[3,4] have highlighted the potential diagnostic role of thin-section CT scanning in identifying nonsolid components of adenocarcinoma of the lung. The nonsolid component is larger in patients with noninvasive tumors and has been shown to discriminate between patients with noninvasive tumors and patients with advanced tumors with a high degree of power.[5] In addition, the proportion of the tumor occupied by the nonsolid component correlates well with the absence of vascular or lymphatic invasion and with better outcome.[6–10] Thus, identification of the size of the nonsolid component on CT scan images of lung adenocarcinoma is a potential surrogate measurement for tumor aggressiveness.

The reliability of almost all data on the proportion

*From the Division of Diagnostic Radiology (Drs. Tateishi, Yonemori, Satake, and Arai), National Cancer Center Hospital, Tokyo, Japan; the Department of Biostatistics (Dr. Uno), Harvard School of Public Health, Boston, MA; and the Division of Biostatistics (Takeuchi), Kitasato University Graduate School, Tokyo, Japan.

Dr. Uno received support for this research by Banyu Life Science Foundation International.

Manuscript received January 12, 2005; revision accepted May 4, 2005.

Correspondence to: Ukihide Tateishi, MD, PhD, Division of Diagnostic Radiology, National Cancer Center Hospital, Tsukiji, Chuo-Ku, 104-0045, Tokyo, Japan; e-mail: utateish@ncc.go.jp

occupied by the nonsolid component is limited, because the investigators assumed that the lesions were spherical and used the maximum cross-sectional diameter on CT scan images to calculate it,[5,6] and the only large series to date used the maximum cross-sectional area of the tumor to predict invasion.[11] To our knowledge, few studies have used CT scanning to calculate the volume of the nonsolid component within tumors and to correlate the proportion occupied by the nonsolid component with pathologic characteristics of tumor invasion. Moreover, most studies to date have proposed diagnostic criteria for lesions without testing their diagnostic validity.[6–11]

We therefore conducted both a derivation and validation cohort study of patients with adenocarcinoma of the lung in order to predict tumors without vessel invasion. Our results will assist physicians in estimating more accurately the probability of a tumor being unassociated with vessel invasion and to decide whether further investigation is necessary to rule the presence of a noninvasive tumor in or out.

Materials and Methods

A retrospective review of the pathologic records for the period between October 2001 and January 2004 identified 288 who had been patients treated for adenocarcinoma of the lung the maximum dimension of which was < 2 cm. A consecutive subset of 288 patients contributed to the derivation analysis and the cross-validation analysis based on the leave-one-out method. The study population consisted of 113 men and 175 women, and their mean age was 64.7 years (age range, 41 to 86 years). All patients had undergone surgical resection consisting of wedge resection or lobectomy. Complete dissection (n = 96; 33%) and sampling of mediastinal or hilar lymph nodes (n = 192; 67%) were performed. The nodes included high and low ipsilateral, paratracheal, subcarinal, and inferior pulmonary ligament lymph nodes, and any other suspicious lymph nodes identified at surgery. Surgical specimens were fixed in formalin and embedded in paraffin. Four-micrometer sections were stained with hematoxylin and eosin and elastica-van Gieson stain. Tumors without vessel invasion were diagnosed when no lymphatic or blood vessel invasion was identified within the lesion microscopically. Based on the current international TNM classification for staging lung cancer,[12] 274 tumors (95%) were classified as stage Ia, and the other 14 tumors (5%) were classified as stage IIa. The clinical records of all patients were available for review. No patients were lost to follow-up, which began on the date of the initial operation. The median duration of follow-up was 22 months, and ranged from 1 to 40 months. This study was approved by our institutional review board after confirmation of informed consent by the patients to a review of their records and images.

CT scanning was performed with a multidetector scanner (Aquilion V-detector; Toshiba Medical Systems; Tokyo, Japan) by using axial 2.0-mm × 4 or 1.0-mm × 16 modes (*ie*, 4 or 16 images per gantry rotation), 120 kVp, 200 to 250 mA, and a 0.5-s scanning time. Thin-section CT scan images were obtained using 2.0-mm sections that were reconstructed at 2.0-mm intervals by means of a high-spatial frequency algorithm and were retrospectively retargeted to each lung with a 20-cm field of view. All images were displayed at window settings for lung (center, −600 Hounsfield units; width, 2,000 Hounsfield units). Image viewing and manipulation were controlled with a workstation (ZIOSOFT M900, Quadra, version 3.10f; ZIOSoft Inc; Tokyo, Japan) that allows the reader to draw lines through regions of interest and the perimeters around them.

The CT scan images were assessed in random order by two independent observers without reference to the clinical findings. The observers examined the images for the following: maximum tumor diameter; nodular edge (irregular or not); presence of a nonsolid component; presence of an air-bronchogram; presence of cavitation, lobulation, pleural indentation, bubble-like lucencies, spiculation, vascular convergence, bronchiectasis, or bronchiolectasis; and the lobe in which the lesion was located (*eg*, upper, middle, or lower). *Nonsolid component* was defined as an area of ground-glass attenuation or hazy increased parenchymal attenuation without obscuring of the underlying vascular markings. We distinguished between *nonsolid tumors* and *part-solid tumors*, with the former being defined as tumors containing only a nonsolid component, and the latter as tumors that contained a partially solid component. Bubble-like lucencies were diagnosed when there were multiple cystic air spaces measuring ≤ 5 mm in diameter within the lesion surrounded by a wall of variable thickness.[13] After an initial independent evaluation, the two observers reviewed all cases in which their interpretations disagreed and reached a final decision by consensus.

The volume of each tumor was calculated by the perimeter method.[14–16] The cross-sectional areas of the entire tumor and of the solid component were calculated by a workstation that manipulates a voxel matrix of 512 × 512 pixels. Two board-certified radiologists who were experienced with image-viewing and image-manipulation software drew a line around the perimeter of each tumor twice. The total tumor volume and the volume of the solid component were calculated by summing the cross-sectional areas and multiplying by the section increment. The volume of the nonsolid component was calculated by subtracting the volume of the solid component from the total volume. The averages of the two volume values calculated by each of the two observers were used in the analyses.

Statistical Analysis

Interobserver variation in relation to CT scan findings was quantified as the weighted κ coefficient of agreement. The predictive performance of volumetric data was evaluated by receiver operating characteristic (ROC) analysis, and the areas under curve were represented by the Az values, which are a measure of diagnostic power represented by the area under the curve.[17,18] A stepwise procedure was used in the logistic regression analysis to select the independent variables that should have been included in the model to predict tumors without vessel invasion. A variable was entered into the model if the probability of its score statistic was < 0.05. The odds ratio (OR) and 95% confidence interval (CI) for the multivariate predictors were estimated. The Hosmer-Lemeshow test was also performed to evaluate goodness-of-fit.[19] Calibration curves comparing the observed proportion of tumors without vessel invasion with the probability of tumors without vessel invasion ordered by the increasing probability of tumors without vessel invasion were constructed. The performance of the learned model was verified by using the leave-one-out cross-validation method, in which all cases but one were used to train the prediction rule, which was then applied to the single excluded case.[20–22] This procedure was repeated for each case, until each case had been left out only once. Cross-validation accuracy was calculated by comparing the predicted response and the observed response.[23] The following variables were considered for their prognostic value: age; gender;

Table 1—*Patient Demographics**

Characteristics	No Vessel Invasion (n = 128)	Vessel Invasion (n = 160)
Gender		
Male	39 (30)	74 (46)
Female	89 (70)	86 (54)
Age,† yr		
Mean	64	65.4
SD	9.1	8.8
Range	41–84	41–86
Location of tumor		
Upper lobe	78 (61)	91 (57)
Middle lobe	14 (11)	5 (3)
Lower lobe	36 (28)	64 (40)
Tumor size,† mm		
Mean	12.4	15.8
SD	4.5	3.5
Range	5.0–20.0	7.0–20.0
Tumor with nonsolid component	124 (97)	78 (49)
Nonsolid tumor	81 (63)	1 (1)
Part-solid tumor	43 (34)	77 (48)
Solid tumor	4 (3)	82 (51)

*Values are given as No. (%).

†The differences between two groups were assessed by a two-sample *t* test. The two tumor subgroups differed significantly in terms of gender (p 0.01 [χ^2 test]). Tumors without vessel invasion were significantly more frequent (p 0.01 [χ^2 test]) in the upper lobe than those with vessel invasion. Tumor size was significantly smaller in tumors without vessel invasion (p 0.01 [*t* test]) than that in tumors with vessel invasion. Tumors with a nonsolid component were significantly more frequent (p 0.0001 [χ^2 test]) among tumors without vessel invasion.

presence or absence of vessel invasion; tumor size; total tumor volume; the volume of the nonsolid component; the proportion occupied by the nonsolid component; and CT scan findings. Univariate analysis was performed by comparing Kaplan-Meier disease-free or recurrence-free survival curves and carrying out log-rank tests. All analyses were conducted using a statistical software package (SAS, version 8.2; SAS Institute, Cary, NC; and R software, version 1.9.0; R project, Center for Computational Intelligence; Vienna, Austria).

Results

The clinical characteristics and outcomes of all patients with adenocarcinoma of the lung are summarized in Table 1. The pathologic diagnosis was lung adenocarcinoma with vessel invasion in 160 of the 288 patients (55.6%), and without vessel invasion in the other 128 patients (44.4%). Female patients had a predilection for tumors without vessel invasion according to the results of the univariate analysis. The median age at presentation was 66 years (age range, 41 to 86 years). Age was not statistically associated with tumor type. Most tumors (n = 169; 58.7%) were in the upper lobe. The median tumor size was 15.0 mm (range, 5.0 to 20.0 mm). Tumors with vessel invasion were significantly larger than tumors without vessel invasion. Among the tumors without vessel invasion, nonsolid tumors (n = 81; 28.1%) were more common than part-solid or solid tumors (n = 47; 16.3%); whereas, among the tumors with vessel invasion, solid or part-solid tumors (n = 159; 55.2%) were more common than nonsolid tumors (n = 1; 0.3%). Tumors with a nonsolid component were more common among the tumors without vessel invasion than among the tumors with vessel invasion.

There was good interobserver agreement in the analysis of the CT scan findings (weighted κ coefficient, 0.63 to 0.79). The following CT scan findings were more frequently identified in tumors with vessel invasion than in tumors without vessel invasion according to the univariate analysis: cavitation; air bronchogram;

Table 2—*Summary Statistics of Volumetric Measurements**

Variables	No Vessel Invasion	Vessel Invasion
Tumor volume, mm^3		
Mean	1,155.7	1,773.6
SD	1,411.1	1,321.3
Q1-Median-Q3	247.6–713.8–1,544.6	867.1–1,492.5–2,367.4
Range	43.6–6,828.0	120.8–6,912.2
Volume of nonsolid component, mm^3		
Mean	1,027.5	496.9
SD	1,372.7	829.6
Q1-Median-Q3	157.5–567.7–1,413.3	0.0–0.0–658.5
Range	0.0–6,593.4	0.0–4583.6
Proportion of nonsolid component, %		
Mean	88.1	24.3
SD	26.4	33.2
Q1-Median-Q3	93.4–100.0–100.0	0.0–0.0–41.4
Range	0.0–100.0	0.0–100.0

*The differences between two groups were assessed by the Wilcoxon two-sample *t* test. The tumor subgroups differed significantly in terms of the volume of those three kinds of measurements (p 0.0001). Q1 = 25th percentile; Q3 = 75th percentile.

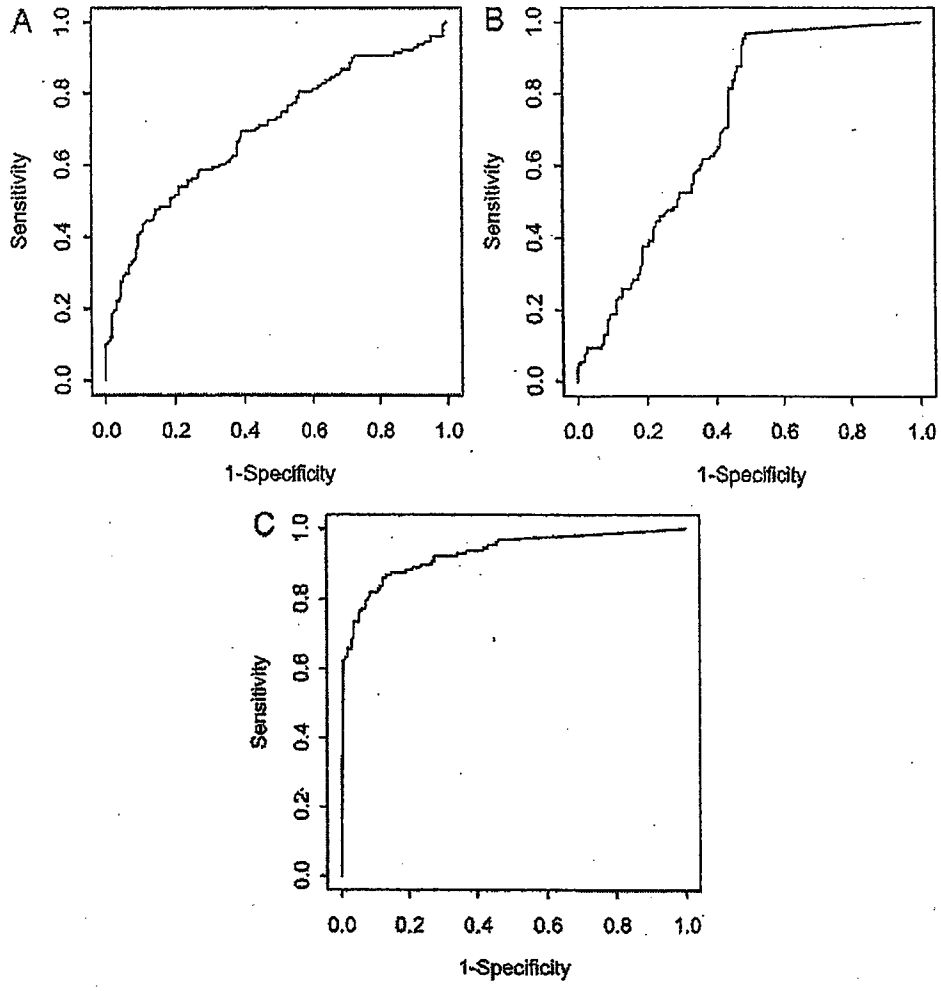

FIGURE 1. *Top, A*: ROC curve for total tumor volume determined by the perimeter method. The mean (± SE) Az value was 0.699 ± 0.030. *Middle, B*: the ROC curve for the volume of the nonsolid component determined by the perimeter method. The mean Az (± SE) value was 0.714 ± 0.030. *Bottom, C*: ROC curve for the proportion occupied by the nonsolid component determined by the perimeter method. The mean Az (± SE) value was 0.928 ± 0.015.

irregular margin; speculation; lobulation; and bronchiectasis or bronchiolectasis. Irregular margins were common in tumors without vessel invasion but were more frequent in tumors with vessel invasion. Vascular convergence was a less common finding and was noted only in patients with tumors that were associated with vessel invasion. Bubble-like lucencies were observed in one tumor with vessel invasion and in one tumor without vessel invasion.

Volumetric Analysis

The results of the volumetric analysis are summarized in Table 2. The median total tumor volume, the median volume of the nonsolid component, and the median proportion occupied by the nonsolid component were 1,123.7 mm^3 (range, 43.6 to 6,912.2 mm^3), 253.4 mm^3 (range, 0 to 6,593.4 mm^3), and 58.0% (range, 0 to 100%), respectively. Significant differences were found between the mean values for total volume and the proportion values in two groups. The ROC analyses to predict tumors without vessel invasion revealed that Az values of total tumor volume, the volume of the nonsolid component, and the proportion occupied by the nonsolid component were 0.699 (95% CI, 0.638 to 0.760), 0.714 (95% CI, 0.653 to 0.775), and 0.928 (95% CI, 0.895 to 0.961), respectively (Fig 1). The potential predictors of tumors without vessel invasion at the threshold of each median value were as follows: total tumor volume; the volume of the nonsolid component; and the proportion occupied by the nonsolid component (Table 3). Univariate analysis showed that our pre-

Table 3—*Potential Predictors of Tumors Without Vessel Invasion**

Criteria	Proportion of Tumors Without Vessel Invasion, %	OR	95% CI	p Value†
Gender		1.9636	1.2053–3.1992	0.0064
Female	50.9			
Male	34.5			
Age		1.1124	0.6983–1.7723	0.6543
≤ 66 yr	45.7			
> 66 yr	43.1			
Tumor size		4.0588	2.4416–6.7472	< 0.0001
≤ 15 mm	58.5			
> 15 mm	25.8			
Air bronchogram		0.1143	0.0585–0.2235	< 0.0001
Positive	13.6			
Negative	58.0			
Irregular margin		0.1605	0.0636–0.4049	< 0.0001
Positive	40.1			
Negative	80.6			
Spiculation		0.0349	0.0159–0.0767	< 0.0001
Positive	7.1			
Negative	68.6			
Lobulation		0.1496	0.0185–1.2122	0.0412
Positive	11.1			
Negative	45.5			
Pleural indentation		0.1148	0.0673–0.1961	< 0.0001
Positive	21.2			
Negative	70.1			
Bubble-like lucencies		1.2540	0.1742–9.0269	0.8221
Positive	50.0			
Negative	44.4			
Vascular convergence		NA	NA	< 0.0001
Positive	0.0			
Negative	50.0			
Bronchiectasis or bronchiolectasis		0.2150	0.0468–0.9882	0.0312
Positive	15.4			
Negative	45			
Tumor volume		2.9934	1.8465–4.8528	< 0.0001
≤ 1,123.7 mm^3	57.6			
> 1,123.7 mm^3	31.3			
Volume of nonsolid component		2.6535	1.6431–4.2853	< 0.0001
> 253.4 mm^3	56.3			
≤ 253.4 mm^3	32.6			
Proportion of nonsolid component		42.778	21.5856–84.7761	< 0.0001
> 80%	84.6			
≤ 80%	11.4			

*The median value was considered to be a cutoff in age, tumor size, tumor volume, the volume of the nonsolid component, and the proportion of the nonsolid component. NA = not applicable.
†χ^2 test.

dictor of interest, the proportion occupied by the nonsolid component, was highly predictive of tumors without vessel invasion at an OR of 42.8 (95% CI, 21.6 to 84.8) with 80.0% as the threshold value.

Derivation of the Prediction Rule

From the 13 variables that reached the level of statistical significance in the univariate analyses comparing tumors with and without vessel invasion, we excluded location of the tumor because the absolute difference fell within the precision range of the test.

The logistic regression analysis identified the following five significant predictors of tumors without vessel invasion: proportion occupied by the nonsolid component; spiculation; pleural indentation; gender; and tumor size (Table 4). The Az value of the ROC analysis for prediction of a tumor without vessel invasion in the derivation phase was 0.957 (Fig 2). We adopted the threshold that yielded an appropriate tradeoff between sensitivity and specificity (*ie*, probability of a tumor without vessel invasion, 0.5). At that point in the ROC curve, the sensitivity, specificity, accuracy, positive predictive value, and

Table 4—*Significant Predictors of Tumors Without Vessel Invasion*

Variables	Coefficient	OR*	95% CI	p Value
Intercept	−1.6729			
Proportion of nonsolid component > 80% vs ≤ 80%	3.5744	35.673	14.392–88.421	< 0.0001
Positive vs negative spiculation	−2.3889	0.092	0.032–0.261	< 0.0001
Positive vs negative pleural indentation	−1.3982	0.247	0.101–0.602	0.0021
Female vs male gender	1.0056	2.734	1.141–6.551	0.0241
Tumor size ≤ 15 mm vs > 15.0 mm	1.1271	3.087	1.249–7.627	0.0146

*OR was presented to predict tumors without vessel invasion.

negative predictive value of the rule were 88.3%, 91.9%, 90.3%, 89.7%, and 90.7%, respectively. The results of the goodness-of-fit test (χ^2, 3.6563; degrees of freedom, 8; $p = 0.89$) indicated that the observed proportion of patients with tumors without vessel invasion was similar to the predicted proportion in the derivation group. The calibration curves for the derivation data demonstrated good calibration of the prediction rule.

Cross-Validation Accuracy

When the rule derived from the 288 patients was applied to the leave-one-out cross-validation cohort, the validation accuracy based on the leave-one-out method was 90.3%, which was quite similar to the model accuracy, suggesting that the rule that was derived to predict tumors without vessel invasion is stable.

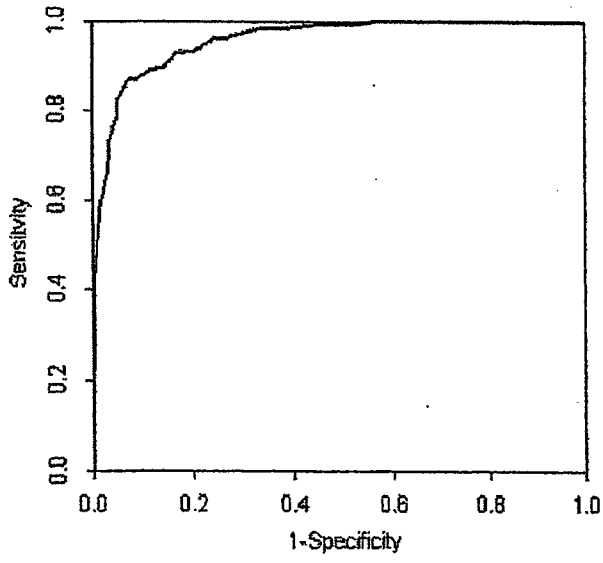

FIGURE 2. ROC curve for the derived model to predict tumor without vessel invasion. The probability of the occurrence of a tumor without vessel invasion based on the derived model can be considered diagnostic, and the tradeoff between sensitivity and specificity at various thresholds of the probability of a tumor without vessel invasion is given by the ROC curve.

Prognostic Analysis

At the last follow-up, 1 of the 288 patients (0.3%) had died, 12 patients (4.2%) were alive with recurrent disease, and the 5-year overall survival rate was 98.7%. Univariate analysis revealed that none of the variables had a significant impact on overall survival. The 5-year recurrence-free survival rate was 83.5%. The patients with tumors without vessel involvement had a 5-year recurrence-free rate of 88.0%, which was significantly better than the rate of 74.6% among the patients with vessel invasion ($p < 0.05$). Cavitation and vascular convergence were significantly associated with recurrence-free survival according to the univariate analysis ($p < 0.01$).

DISCUSSION

The proportion occupied by the nonsolid component is characteristically higher in patients with lung adenocarcinoma without vessel invasion, and several studies[4,5] have demonstrated that it distinguishes tumors without vessel invasion from tumors with vessel invasion. Nevertheless, controversy remains regarding its reproducibility in optimally distinguishing tumors without vessel invasion from tumors with vessel invasion. In this study, we investigated the diagnostic capacity of the proportion occupied by the nonsolid component to predict tumors without vessel invasion in a well-characterized study population.

We performed ROC analysis to assess the ability of the proportion occupied by the nonsolid component to discriminate between tumors with and without vessel invasion. We have documented that the diagnostic probability of the proportion occupied by the nonsolid component for tumors without vessel invasion is accurate. The Az value observed for the proportion occupied by the nonsolid component was 0.957. In our study population, its discriminatory capacity yielded positive and negative predictive values for tumors without vessel invasion of 89.7% and 90.7%, respectively. These observations suggest that the identification of the proportion occupied by the nonsolid component on CT images may be useful

for predicting tumors without vessel invasion in patients with adenocarcinoma of the lung.

At both baseline screenings and repeat CT screenings for lung cancer, tumors containing a nonsolid component have been found to be a significant sign of malignancy.[24] Henschke and colleagues[25] found that 19% of the 233 cases with positive results at baseline screening had a tumor with the nonsolid component and that the tumors were predominantly bronchioloalveolar carcinoma and adenocarcinoma with bronchioloalveolar carcinoma features. These predominant histologic types of malignancy corresponded to noninvasive and invasive tumors of lung adenocarcinoma. The quantification of the extent or growth rate of the solid and nonsolid components of tumors is necessary during CT scan screening for lung cancer.

Swensen and colleagues[18] created a multivariate logistic regression model to predict a malignant solitary pulmonary nodule (SPN) in a derivation and validation analysis. Of 629 radiologically intermediate nodules in their study, 23% were malignant SPNs. The investigators identified the following three independent findings that predicted malignant SPNs: upper lobe distribution; tumor size; and spiculation. Among these findings, spiculation was associated with the prediction model in our results. Pleural indentation and male predilection were also significant predictors of tumors with vessel invasion in our study.

Some studies[26–28] using the segmentation algorithm of software have yielded calculations of tumor volume in three dimensions. The excellent interobserver variability suggests that tumor volume estimations by different observers can be reliably compared when three-dimensional volumetric software is used. However, this technique does not enable the segmentation of tumors that contain a nonsolid component.[27,28] Since most tumors in our study contained a nonsolid component and were not appropriate for three-dimensional volumetric analysis, tumor volume was calculated by the perimeter method, which had potential sources of error that affected the results of volumetric analyses.[29]

The proportion occupied by the nonsolid component was dichotomized using the median value for a threshold level in the univariate and multivariate analyses performed. In both the univariate and multivariate analyses, the proportion occupied by the nonsolid component yielded the highest point estimates and CIs for the ORs of tumors without vessel invasion. However, it should be noted that there was enough of a difference between the values for patients in whom the nonsolid component occupied a high proportion of the tumor and those for patients in whom the nonsolid component occupied a small proportion of the tumor that similar results could have been obtained with different threshold values.

There are other potential limitations of this study. The size of the sample may also have led to false-positive results because of the number of covariates included in the initial analysis. However, the strength of the association with our primary outcome of interest, as well as the historical precedence of other significant predictors in our multivariate analysis, lends credence to our conclusions. In summary, the results of our study confirm that the proportion occupied by the nonsolid component of a tumor on CT scans is a reliable predictor of tumors without vessel invasion with much greater confidence than was possible in the past.

References

1 Travis WD, Colby TV, Corrin B, et al. Histological typing of lung and pleural tumors. Berlin, Germany: Springer, 1999

2 Noguchi M, Morikawa A, Kawasaki M, et al. Small adenocarcinoma of the lung: histologic characteristics and prognosis. Cancer 1995; 75:2844–2852

3 Jang HJ, Lee KS, Kwon OJ, et al. Bronchioloalveolar carcinoma: focal area of ground-glass attenuation at thin-section CT as an early sign. Radiology 1996; 199:485–488

4 Kuriyama K, Seto M, Kasugai T, et al. Ground-glass opacity on thin-section CT: value in differentiating subtypes of adenocarcinoma of the lung. AJR Am J Roentgenol 1999; 173:465–469

5 Ohde Y, Nagai K, Yoshida J, et al. The proportion of consolidation to ground-glass opacity on high resolution CT is a good predictor for distinguishing the population of non-invasive peripheral adenocarcinoma. Lung Cancer 2003; 42: 303–310

6 Aoki T, Tomoda Y, Watanabe H, et al. Peripheral lung adenocarcinoma: correlation of thin-section CT findings with histologic prognostic factors and survival. Radiology 2001; 220:803–809

7 Suzuki K, Yokose T, Yoshida J, et al. Prognostic significance of the size of central fibrosis in peripheral adenocarcinoma of the lung. Ann Thorac Surg 2000; 69:893–897

8 Kodama K, Higashiyama M, Yokouchi H, et al. Prognostic value of ground-glass opacity found in small lung adenocarcinoma on high-resolution CT scanning. Lung Cancer 2002; 33:17–25

9 Matsunaga H, Yokoi K, Anraku M, et al. Proportion of ground-glass opacity on high-resolution computed tomography in clinical T1N0M0 adenocarcinoma of the lung: a predictor of lymph node metastasis. J Thorac Cardiovasc Surg 2002; 124:278–284

10 Kim EA, Johkoh T, Lee KS, et al. Quantification of ground-glass opacity on high-resolution CT of small peripheral adenocarcinoma of the lung: pathologic and prognostic implications. AJR Am J Roentgenol 2001; 177:1417–1422

11 Takashima S, Maruyama Y, Hasegawa M, et al. Prognostic significance of high-resolution CT findings in small peripheral adenocarcinoma of the lung: a retrospective study on 64 patients. Lung Cancer 2002; 36:289–295

12 Lababede O, Meziane MA, Rice TW. TNM staging of lung cancer: a quick reference chart. Chest 1999; 115:233–235

13 Adler B, Padley S, Miller RR, et al. High-resolution CT of bronchioloalveolar carcinoma. AJR Am J Roentgenol 1992; 159:275–277

14 Winter-Muram HT, Jennings SG, Tarver RD, et al. Volumetric growth rate of stage I lung cancer prior to treatment: serial CT scanning. Radiology 2002; 223:798–805
15 Winter-Muram HT, Jennings SG, Meyer CA, et al. Effect of varying CT section width on volumetric measurement of lung tumors and application of compensatory equations. Radiology 2003; 229:184–194
16 Jennings SG, Winter-Muram HT, Tarver RD, et al. Lung tumor growth: assessment with CT-comparison of diameter and cross-sectional area with volume measurements. Radiology 2004; 231:866–871
17 Hanley JA, McNeil BJ. The meaning and use of the area under a receiver operating characteristic (ROC) curve. Radiology 1982; 143:29–36
18 Swensen SJ, Silverstein MD, Ilstrup DM, et al. The probability of malignancy in solitary pulmonary nodules: application to small radiologically intermediate nodules. Arch Intern Med 1997; 157:849–855
19 Lemeshow S, Hosmer DW. A review of goodness-of-fit statistics for use in the development of logistic regression models. Am J Epidemiol 1982; 115:92–106
20 Wasson JH, Sox HC, Neff RK, et al. Clinical prediction rules: applications and methodological standards. N Engl J Med 1985; 313:793–799
21 Scott JA. Pulmonary perfusion patterns and pulmonary arterial pressure. Radiology 2002; 224:513–518
22 Arana E, Delicado P, Marti-Bormati L. Validation procedures in radiologic diagnostic models: neural network and logistic regression. Invest Radiol 1999; 34:636–642
23 Stone M. Cross-validatory choice and assessment of statistical predictions. J R Stat Soc B 1974; 36:111–147
24 Henschke CI, McCauley DI, Yankelevitz DF, et al. Early lung cancer action project: overall design and findings from baseline screening. Lancet 1999; 354:99–105
25 Henschke CI, Yankelevitz DF, Mircheva R, et al. CT screening for lung cancer: frequency and significance of part-solid and nonsolid nodules. AJR Am J Roentgenol 2002; 1178: 1053–1057
26 Yankelevitz DF, Reeves AP, Kostis WJ, et al. Small pulmonary nodules: volumetrically determined growth rates based on CT evaluation. Radiology 2000; 217:251–256
27 Revel MP, Lefort C, Bissery A, et al. Pulmonary nodules: preliminary experience with three-dimensional evaluation. Radiology 2004; 231:459–466
28 Revel MP, Bissery A, Bienvenu M, et al. Are two-dimensional CT measurements of small noncalcified pulmonary nodules reliable? Radiology 2004; 231:453–458
29 Staron RB, Ford E. Computed tomographic volumetric calcification reproducibility. Invest Radiol 1986; 21:272–274

Skelet Radiol
DOI 10.1007/s00256-005-0021-0

SCIENTIFIC ARTICLE

Ukihide Tateishi
Tadashi Hasegawa
Takayuki Nojima
Tsutomu Takegami
Yasuaki Arai

MRI features of extraskeletal myxoid chondrosarcoma

Received: 23 February 2005
Revised: 13 May 2005
Accepted: 27 July 2005

All authors of this research paper have directly participated in the planning, execution, or analysis of the study
The contents of this manuscript have not been copyrighted or previously published
There are no directly related manuscripts or abstracts, published or unpublished, by any authors of this paper

U. Tateishi (✉) · Y. Arai
Division of Diagnostic Radiology,
National Cancer Center Hospital,
5-1-1, Tsukiji, Chuo-Ku,
104-0045 Tokyo, Japan
e-mail: utateish@ncc.go.jp
Tel.: +81-3-35422511
Fax: +81-3-35423815

T. Hasegawa
Department of Clinical Pathology,
Sapporo Medical University
School of Medicine,
Sapporo, Japan

T. Nojima
Department of Pathology,
Kanazawa Medical University,
Ishikawa, Japan

T. Takegami
Division of Molecular Oncology
and Virology,
Medical Research Institute,
Kanazawa Medical University,
Ishikawa, Japan

Abstract *Objective:* To describe the MRI features of extraskeletal myxoid chondrosarcoma in comparison with clinicopathologic findings. *Design and patients:* The study comprised 12 male subjects and seven female subjects with a mean age of 53 years (range 16–76 years). MRI findings, evaluated by two radiologists with agreement by consensus, were compared for histopathologic features. *Results:* The tumor size ranged from 2.0 cm to 20.0 cm (mean 8.9 cm). Fusion gene transcripts could be detected in 13 (68%) of the 19 cases: EWS-CHN in nine cases, TAF2N-CHN in three, and TFG-TCH in one. There were six fusion-negative cases. Signal characteristics on T1-weighted and T2-weighted MR images were non-specific with regard to each cytogenetic variant. Peripheral enhancement was seen more frequently in tumors with the EWS-CHN variant than in those with other cytogenetic variants. The characteristic pattern of enhancement corresponded to the presence of fibrous septa and peripheral areas of high cellularity within lobules, by correlation with pathologic findings. All cases with TAF2N-CHN or TFG-TCH variants showed invasion of extracompartmental structure, bone, or vessels. *Conclusion:* Extraskeletal myxoid chondrosarcoma is an uncommon soft-tissue malignancy that may be recognized by MRI features of multilobular soft-tissue mass often invading extracompartmental, bony, and vascular structures.

Keywords Extraskeletal myxoid chondrosarcoma · MRI · Cytogenetic variant

Introduction

Extraskeletal myxoid chondrosarcoma (EMC) is a rare malignant soft-tissue tumor characterized by abundant myxoid matrix and malignant chondroblastic cells [1, 2]. EMC mostly arises in the deep soft tissue of the proximal extremities and limb girdles and comprises multiple gelatinous nodules divided by fibrous septa. Although the most common manifestation is an enlarging soft-tissue mass, some lesions are accompanied by pain and tenderness or may restrict the range of motion. Long-term follow-up studies have shown that EMC is a slowly growing tumor with a risk of local recurrence or distant metastasis. EMC is a tumor with long survival but is known to have a potential for local recurrence, metastasis, and a disease-associated death [1–4].

EMC was described as a distinct entity, precisely, by Enzinger and Shiraki [5]. Subsequent clinicopathologic